The nanoscale mobility of calcium channels is driven by readily releasable synaptic vesicles to support precise neurotransmission in live *C. elegans*

Yunke Zhao[1*], Dai Zhai[1] and Fabien Pinaud[1,2*]

[1]Department of Biological Sciences, University of Southern California, 1050 Child Way, Los Angeles, CA 90089, USA.

[2]Department of Physics and Astronomy, University of Southern California, 1050 Child Way, Los Angeles, CA 90089, USA.

*Correspondence should be addressed to Y.Z. (yunkezha@usc.edu) and F.P. (pinaud@usc.edu)

Abstract

Precise neurotransmission requires voltage-gated calcium channels (VGCCs) to be tightly coupled with synaptic vesicles (SVs) at active zones (AZs). As VGCCs are mobile in the fluid presynaptic membrane, it remained unclear how they spatiotemporally align with SVs for reliable synaptic release. Using super-resolution imaging and single-molecule tracking in *C. elegans*, we report that two diffusive behaviors of N-type VGCCs at AZs are governed by primed SVs via distinct mechanisms. VGCCs diffuse slowly in multiple nanodomains (~100 nm) that spatially correlate with UNC-10/RIM, and the channel mobility and nanodomain numbers are coupled to SNAREs assembly and SV priming levels via RAB-3/UNC-10/UNC-13L tripartite complexes. Outside nanodomains, a faster mobility of VGCCs and their AZ distribution scale with UNC-13S-mediated priming under an antagonistic regulation by UNC-10 and TOM-1/Tomosyn. These findings reveal unexpected mechanisms whereby pools of readily releasable SVs actively control the nanoscale mobility and nanodomain organization of VGCCs to support precise neurotransmission.

Keywords

Nanoscale diffusion, Super-resolution imaging, Voltage-gated calcium channels, Active zone, Synaptic vesicle release, UNC-10, UNC-13, SNARE

Introduction

At the presynaptic active zone (AZ), exocytosis of synaptic vesicles (SVs) is spatiotemporally orchestrated by an evolutionarily conserved release machinery[1–3] that includes multi-subunits voltage-gated calcium channels (VGCCs), which provide crucial calcium influx for SV release[4,5]. In both mammals and *C. elegans* nematodes, VGCCs are recruited in close proximity to SVs mainly by the AZ modulator UNC-10/RIM, which interacts with the channel's α1 pore-forming subunit UNC-2/Ca_v2 and binds vesicular Rab-3 to dock SVs[6–9]. UNC-10/RIM also directly regulates UNC-13/Munc-13, which primes SVs to become readily releasable[10–12]. During priming, UNC-13/Munc-13 tethers SVs to the plasma membrane and coordinates the assembly of SNARE complexes by conformationally opening and aligning UNC-64/Syntaxin-1 (t-SNARE) with both SNAP-25 (t-SNARE) and vesicular SNB-1/VAMP (v-SNARE), which drive SV fusion upon calcium entry[13–16]. By interacting with UNC-13/Munc-13, UNC-10/RIM couples VGCCs to readily releasable SVs, awaiting calcium influx[17]. The local density of VGCCs and their coupling distances to SVs are therefore key determinants of the SV release probability and its efficacy[18,19]. Indeed, synapses having slow release kinetics are characterized by a relatively broad, microdomain coupling between VGCCs and SVs (>100 nm), while fast-releasing synapses adopt a much narrower, nanodomain coupling (<100 nm)[20,21].

While precise spatial coupling between VGCCs and SVs is critical for efficient neurotransmissions, maintaining such nanoscale proximities is complicated by the lateral diffusion of VGCCs in the fluid presynaptic membrane, as observed in diverse synaptic systems[22–24]. Indeed, the mobility of VGCCs at AZs has emerged as a new determinant of presynaptic release, with VGCC mobilities scaling with intracellular calcium levels and neural activities, and alteration of channel diffusion shaping short-term synaptic plasticity and homeostasis[23–25]. Because VGCCs are not static, one would expect their coupling distances to SVs and release probabilities to shift continuously. How the AZ organization maintains precise spatiotemporal coupling between mobile VGCCs and SVs for reliable synaptic releases remains unclear.

Here, we describe how readily releasable SVs actively drive the nanoscale mobility and spatial organization of N-type VGCCs within intact neuromuscular synapses of live *C. elegans*. Using single particle tracking and super-resolution imaging, we characterized two distinct diffusive behaviors of VGCCs at AZ. We show that VGCCs diffuse slowly within multiple intra-AZ nanodomains (∼100 nm) that are organized in the typical dense-projection-like landscape of *C.*

68 *elegans* and that spatially correlate with UNC-10. Outside these nanodomains, the channels adopt
69 a faster diffusion mode while being confined within the larger, diffraction-limited AZ puncta (~300
70 nm). We further show that the two mobilities of VGCCs are governed by SV priming and SNARE
71 complex assembly under the coordination of UNC-10, but by different UNC-13 isoforms.
72 Specifically, the slow mobility and nanodomain number of VGCCs are predominantly regulated
73 by UNC-13L-mediated priming through tripartite SV coupling complexes involving RAB-3,
74 UNC-10 and UNC-13L, while the fast mobility and AZ distribution of VGCCs outside
75 nanodomains scale with the pool of UNC-13S-primed SVs under antagonistic regulations by
76 UNC-10 and the t-SNAREs inhibitor TOM-1/Tomosyn. We propose that the heterogeneous
77 mobilities and spatial organizations of N-type VGCCs provide distinct channel-vesicle coupling
78 strategies for different pools of readily releasable SVs, offering a tunable mechanism to set SV
79 release probabilities.
80
81 **Result**
82 **N-type VGCCs exhibit two distinct confined diffusive behaviors in live *C. elegans***
83 At neuromuscular junction (NMJ) synapses in *C. elegans*, the single N- and P/Q-type VGCCs
84 (UNC-2/Cav2) mediate both evoked and tonic synaptic releases[26]. The functions and surface
85 trafficking of UNC-2/Cav2 require the extracellular α2δ subunit UNC-36, whose own AZ
86 localization also depends on UNC-2/Cav2[26–28]. To study the dynamic distributions and nanoscale
87 mobilities of VGCC complexes, we used complementation activated light microscopy (CALM)
88 with single molecule sensitivity in intact living *C. elegans*[29,30]. We endogenously tagged UNC-
89 36/α2δ with a N-terminal dark split sfCherry1-10[31] (sCherry-UNC-36) using CRISPR/Cas9[32]. To
90 activate the fluorescent signals of the extracellular-facing sCherry-UNC-36, we introduced a
91 synthetic complementary peptide (sfCherry11) via pseudocoelomic microinjections[29,30], which
92 allows for specific detections of surface VGCC without interference from intracellular background
93 signals (Fig. 1a). We previously reported that N-terminal tagging of split-fluorescent proteins to
94 UNC-36/α2δ does not alter the conducting activities of VGCCs[29] and animals expressing sCherry-
95 UNC-36 had functional channels and exhibited normal locomotion compared to N2 Bristol wild-
96 type (WT) animals[33] (Fig. S1a). After fluorescence activation by CALM, surface sCherry-UNC-
97 36 showed puncta localization along the nerve cords as reported[29] and colocalized with
98 endogenous UNC-2/Cav2[27] (Fig. 1b; Fig S1b). To further confirm the AZ localization of sCherry-

99 UNC-36, we endogenously tagged the AZ marker UNC-10/RIM with 5xMyc and UNC-2/Cav2
100 with HA at the N-terminus. Those transgenic animals showed normal locomotion and synaptic
101 release compared to WT (Fig. S1c and S1d). Consistent with previous findings[9,27,28], N-type
102 VGCCs puncta represented by either surface sCherry-UNC-36 or HA-UNC-2 colocalized with
103 Myc-UNC-10 puncta at AZs, and overlapped with NMJ boutons along the nerve cords (Fig. S1e
104 and S1f).
105 In *C. elegans*, UNC-36/α2δ is also required for the function of L-type Egl-19/Cav1 channels in
106 muscles, but is dispensable for Egl-19/Cav1-mediated tonic releases at NMJs[26,34]. To test whether
107 synaptic sCherry-UNC-36 also represents L-type VGCCs, we probed the extent to which UNC-
108 36/α2δ colocalizes with Egl-19/Cav-1 at nerve cords versus muscles. In contrast to UNC-2/Cav2,
109 endogenous Egl-19/Cav1[35] showed a broad distribution along nerve cords, with little co-
110 localization with either GFP-UNC-2 or surface sCherry-UNC-36 (Fig. S1f-S1h). This is consistent
111 with previous findings that UNC-2/Cav2 and Egl-19/Cav1 localize to distinct synaptic regions[36,37]
112 and aligns with the reported function of UNC-36/α2δ, which is required for UNC-2/Cav2 but not
113 Egl-19/Cav1 mediated synaptic releases at NMJs[26]. The dispersed distribution of neuronal Egl-
114 19/Cav1 was also in stark contrast to the puncta distribution of muscular Egl-19/Cav1, which
115 extensively colocalized with surface sCherry-UNC-36 at the sarcolemma of muscles[29,30,34] (Fig.
116 S1i and S1j). Together, these results indicate that UNC-36/α2δ is predominantly associated with
117 UNC-2/Cav2 at AZs rather than with Egl-19/Cav1.
118 To track individual VGCCs by CALM, the sub-diffraction localizations of single sCherry-UNC-
119 36 signals were extracted with a precision of ~20 nm and linked frame to frame to construct the
120 diffusion trajectory[38] of each channel (Fig. 1b; Fig. S2a). At AZs, individual VGCCs exhibited
121 heterogeneous diffusion dynamics with single-step sizes ranging from a few tens to hundreds of
122 nanometers per frame (Fig. 1b; Fig. S2b; Movie S1-S2). To quantitatively define these different
123 mobilities, we analyzed pooled trajectories (n=42,391 from 58 animals) based on the probability
124 distribution of their squared displacements[29,30,39]. We found that VGCCs have two distinct
125 confined diffusive behaviors at AZs in live *C. elegans* (Fig. 1c). The major fraction of VGCC
126 (81%) exhibited a slow mobility, with a diffusion coefficient D_{slow} of 0.0075 ± 0.0010 $\mu m^2/s$ and
127 were confined within circular nanodomains 104 ± 23 nm in diameter. The remaining 19% of
128 VGCCs displayed a five-fold faster diffusion (D_{fast} = 0.038 ± 0.008 $\mu m^2/s$) and were confined
129 within larger domains 289 ± 29 nm in diameter (Fig. 1c). Within individual VGCC trajectories,

130 alternations between slow and fast diffusions were observed (Fig. 1d; Fig. S2c), indicating that
131 D_{slow} and D_{fast} represent two diffusive behaviors of single channels rather than two independent
132 populations of VGCCs. Later observations also show that removal of AZ proteins that directly
133 interact with UNC-2 alters both diffusions, supporting that D_{fast} reflects a genuine faster mobility
134 of VGCC complexes rather than a transient dissociation of UNC-36 from UNC-2. While these
135 alternating diffusive behaviors of VGCCs in *C. elegans* are unique, their respective diffusion
136 coefficients are similar to those of Cav2 in different organisms. For instance, D_{slow} matches the
137 mean diffusion coefficient reported for Cac/Cav2 in *Drosophila* NMJs (0.0075 $\mu m^2/s$)[25], while
138 D_{fast} is similar to the mobility reported for Cav2.1 in rodent hippocampal synapses (0.04 $\mu m^2/s$)[23].
139 The small confinement size of VGCCs falls between those measured for rodent Cav2.1 (~80 nm)[23]
140 and Drosophila Cac/Cav2 (~117 nm)[25], while their larger confinement matches the expected size
141 of AZ in *C. elegans*[40]. This suggests that the nanoscale mobilities of VGCCs reflect intrinsic
142 structural features of AZs[41], which we studied next.
143

144 **N-type VGCCs diffuse in multi-nanodomains that spatially correlate with UNC-10/RIM at**
145 **AZs**

146 The hallmark of *C. elegans* AZ is an electron dense projection (DP) with branched ultrastructure
147 and ~ 100 nm bay-like sites for SV docking and release[42,43]. We therefore determined whether the
148 confinement of VGCCs in nanodomains reflects those AZ sub-structures by resolving the
149 nanoscale distribution of the channels and that of UNC-10 using stimulated emission depletion
150 (STED) microscopy. Interestingly, we found that VGCCs and UNC-10 form multiple co-localizing
151 nanodomains within individual AZ puncta, in agreement with our diffusion analyses (Fig. 1e and
152 1f; Fig. S3a-d). Notably, the spatial organization of these nanodomains closely resembled the bay-
153 like sites between DP branches[42], consistent with the known functions of UNC-10/RIM in docking
154 SVs and coupling VGCCs[1,3,44]. Similar to the variability in the number of docking bays across
155 different DPs[42], we also observed heterogeneities in nanodomain numbers per AZ. Most AZs
156 (~50%) contain 4-5 VGCC or UNC-10 nanodomains, 28-37% contain more than 6 nanodomains,
157 while 15-22% have 1-3 nanodomains (Fig. S3e). Quantitative analyses showed a significant
158 correlation between the numbers of VGCC and UNC-10 nanodomains, both exhibiting a median
159 of five nanodomains per AZ along the dorsal nerve cords (interquartile range [IQR]: 4/6) (Fig.1g).
160 While not strictly identical, the nanodomains of VGCCs and UNC-10 showed similar spatial

161 distribution, with a median nearest neighbor distance (NND) of 105 nm (IQR: 87/122nm) and 106
162 nm (IQR: 90/121nm), respectively (Fig. 1h). The size of VGCC nanodomains (median Area
163 Equivalent Diameter AED: 103 nm; IQR: 88/121nm) also aligned with the size of UNC-10
164 nanodomains (106 nm; IQR: 93/122nm) and importantly, closely matched the confinement size of
165 slow-diffusing VGCCs extracted by diffusion analyses (104 nm ± 23 nm) (Fig. 1c and 1h). This
166 indicates that the slow mobility (81%) of VGCCs reflects their diffusion within individual
167 nanodomains that spatially correlate with UNC-10.
168 Within each AZ, multiple VGCCs or UNC-10 nanodomains form an elliptic punctum similar to
169 the overall DP geometry established by electron microscopy[42,43] (Fig. 1f). The size of VGCC
170 puncta, defined by their long and short axes (median: 334 x 240 nm), strongly correlates with that
171 of UNC-10 (median: 339 x 248 nm) (Fig.1i and 1j; Fig. S3f). To adequately compare these
172 parameters with the circular confinement size of fast-diffusing VGCCs established by diffusion
173 analyses, we also calculated their area equivalent diameter (AED). The median AED of VGCCs
174 was 291 nm (IQR: 260/322nm) and that of UNC-10 was 301 nm (IQR: 265/340nm) (Fig. 1j). Both
175 sizes are consistent with the confined domain (289 ± 29 nm) of fast-diffusing VGCCs, suggesting
176 that the fast mobility (19%) reflects their exploration across the multi-nanodomain AZ area.
177
178 **UNC-10 enhances the diffusion of VGCCs and promotes their multi-nanodomain**
179 **organization**
180 To investigate whether VGCC nanodomains are organized by UNC-10, we examined their
181 nanoscale distribution in an *unc-10(md1117)*[8] null mutant. *Unc-10(md1117)* animals showed
182 severely impaired neurotransmission and fewer VGCC puncta along the nerve cords as previously
183 described[9,45] (Fig. 2a; Fig. S4a-4c). By STED, we found that, in the absence of UNC-10, VGCC
184 nanodomains persist (Fig. 2b), but their median number decreases significantly from 5 to 2 per
185 punctum (Fig. 2c). The percentage of VGCC puncta containing more than 3 nanodomains dropped
186 from 85% in WT animals to 11% in *unc-10(md1117)* mutants (Fig. 2d). Meanwhile, the NND
187 between VGCC nanodomains also significantly increased, resulting in a more dispersed
188 organization compared to WT (Fig. 2e). These results show that, while VGCC nanodomains form
189 independently of UNC-10, UNC-10 promotes their accumulation at AZs and maintains them in a
190 tight spatial organization.

191 We then studied the mobility of individual VGCCs in *unc-10(md1117)* mutants using CALM. The
192 two diffusive behaviors of VGCCs were still observed in these mutants and their relative fractions
193 remained unchanged compared to WT (Fig. 2f), suggesting that UNC-10 does not impact the
194 ability of VGGCs to diffuse inside or outside nanodomains. However, VGCCs were significantly
195 slower in *unc-10(md1117)* mutants, with both D_{slow} within nanodomains and D_{fast} across AZ being
196 reduced by half compared to WT (Fig. 2g). This is consistent with a similar decrease in Cav2
197 diffusion observed after removal of RIM at *Drosophila* NMJs[25]. The channels were also
198 significantly more confined within nanodomains (*unc-10*: 78 ± 23 nm *vs.* WT: 104 ± 23 nm), but
199 their diffusion range across AZ was maintained at WT levels (*unc-10*: 270 ± 28 nm *vs.* WT: 289 ±
200 29 nm) (Fig. 2h). Together, this indicates that UNC-10 enhances the mobilities of VGCCs both
201 inside and outside nanodomains, in addition to its role as a spatial organizer of VGCC
202 nanodomains at AZs.
203
204 **The mobility and spatial organization of nanodomain-associated VGCCs are regulated by**
205 **UNC-10/RIM mediated coupling to synaptic vesicles**
206 To understand how UNC-10, as a cytomatrix protein, enhances the mobility of VGCCs, we
207 investigated whether the channel diffusion reflects their physical coupling to SVs through UNC-
208 10. As UNC-10 docks SVs by binding to vesicular RAB-3[12,46], we examined if the mobility of
209 VGCCs would be impacted in *rab-3(js49)* mutants[46], which have SV docking defect similar to that
210 of *unc-10(md1117)* animals[47,48]. *Rab-3(js49)* mutants exhibited reduced neurotransmission[48],
211 showing impaired locomotion and increased resistance to aldicarb (Fig. 3a and 3b). However, the
212 loss of RAB-3 had no significant influence on the diffusion coefficients of VGCCs, suggesting
213 that docking defects alone do not account for the decreased channel mobilities observed in *unc-*
214 *10(md1117)* mutants (Fig. 3c and 3d; Fig. S5a). UNC-10 also binds the priming factor UNC-
215 13L/Munc-13, which physically bridges SVs with the presynaptic membrane[49,50]. We thus
216 examined the channel mobilities in *unc-10(nu487)* animals carrying K77E/K79E mutations, which
217 disrupt interactions between the ZnF domain of UNC-10 and UNC-13L[11,12,17]. *Unc-10(nu487)*
218 mutants were reported to have reduced release probability[17] and they showed mild uncoordinated
219 phenotypes with near-normal aldicarb-resistance (Fig. 3a and 3b). Again, the diffusion coefficients
220 of VGCCs in these mutants remained similar to WT (Fig. 3c and 3d; Fig. S5b), indicating that
221 dissociating UNC-10 from UNC-13L is not sufficient to reduce the channel mobilities.

222 Interestingly, when both interactions of UNC-10 with RAB-3 and UNC-13L were simultaneously
223 disrupted in *rab-3;unc-10(nu487)* double mutants, VGCCs within nanodomains exhibited
224 significantly reduced diffusion coefficients (D_{slow}) and increased confinement (double mutant: 74
225 ± 23 nm *vs.* WT: 104 ± 23 nm), phenocopying changes observed in *unc-10(md1117)* animals (Fig.
226 3c; Fig. S5c). On the contrary, D_{fast} for VGCCs outside nanodomains remained at WT levels (Fig.
227 3d). This indicates that the two diffusive behaviors of VGCCs are regulated by UNC-10 via distinct
228 mechanisms, with the channel mobility in nanodomains being driven by UNC13L/RAB-3-
229 dependent SV coupling but being independent of SV coupling or of UNC13L/RAB-3 in the rest
230 of the AZ. We note that the larger diffusion range of VGCCs exploring the AZ was differentially
231 impacted in the two single mutants, as it significantly decreased in the absence of RAB-3 (*rab-3*:
232 234 ± 30 nm *vs.* WT: 289 ± 29 nm), but increased in *unc-10(nu487)* mutants (*unc-10*: 322 ± 32 nm
233 vs. WT: 289 ± 29 nm). These opposing effects offset each other in *rab-3;unc-10(nu487)* double
234 mutants, where the diffusion range remained similar to WT (Fig. 3d). This suggests that the AZ
235 area explored by VGCCs outside nanodomains is promoted by UNC-10/RAB-3-mediated SV
236 docking while it is restricted by UNC-10/UNC-13L interactions. In *rab-3;unc-10(nu487)* double
237 mutants, the neurotransmission and locomotion defects were significantly more severe than in both
238 single mutants, suggesting that the interactions of UNC-10 with RAB-3 and UNC-13L are
239 functionally complementary (Fig. 3a and 3b). Together, these findings show that the diffusion of
240 nanodomain-associated VGCCs is driven by a tripartite UNC-10/RAB-3/UNC-13L SV coupling
241 complex, which is essential for efficient synaptic release.
242 To test whether this SV coupling complex also participates in organizing VGCC nanodomains, we
243 examined the distribution of VGCCs in *rab-3;unc-10(nu487)* double mutants by STED. We found
244 that the distribution of VGCC nanodomains became more compact and elongated than in WT
245 animals, with their NND and puncta shape (long/short axes ratio) being significantly altered (Fig.
246 3e-3g). The number of nanodomain per puncta was also significantly reduced, yet it was not
247 impacted to the extent observed in the absence of UNC-10 (Fig. 3h and 3i). This indicates that SV
248 coupling mediated by UNC-10 partially promotes the accumulations of VGCC nanodomains and
249 shapes their spatial organization at AZs.
250
251 **The mobility and AZ organization of VGCCs is governed by synaptic vesicle priming and**
252 **SNARE complex assembly**

253 As UNC-10/UNC-13L interactions couple VGCCs to readily releasable SVs[17], we next
254 investigated whether the channel mobility is regulated by SV priming. We examined the diffusion
255 of VGCCs in *unc-13(s69L-S-)* null mutants, where the absence of both UNC-13 isoforms abolishes
256 SV priming and synaptic release[49,51] (Fig. 4a; Fig. S6a). In *unc-13(s69L-S-)* animals, nanodomain-
257 associated VGCCs exhibited significantly reduced D_{slow} and increased confinement (*unc-13*$^{L-S-}$: 81
258 ± 21 nm *vs.* WT: 104 ± 23 nm), phenocopying changes observed in *rab-3;unc-10(nu487)* double
259 mutants (Fig. 4b; Fig. S6b). Because disrupting the interaction of UNC-13L with UNC-10 in *unc-*
260 *10(nu487)* animals did not influence the channel mobility, these results suggest that VGCC
261 diffusion in nanodomains is impacted by SV priming via both UNC-13L and UNC-13S rather than
262 by simple interaction between UNC-13L and UNC-10. To further test this, we studied the diffusion
263 of VGCCs in *unc-13(e51L-S+)* mutants, where priming levels are slightly restored by endogenous
264 expression of only the UNC-13S isoform, which lacks the UNC-10-binding domain, but contains
265 the core regions required for priming[51]. In *unc-13(e51L-S+)* animals, neurotransmission was
266 significantly improved compared to *unc-13(s69L-S-)* mutants (Fig. 4a; Fig. S6a), but it remained
267 defective compared to WT, consistent with UNC-13L being critical for efficient SV release[17,51].
268 When expressing the UNC-13S isoform, both D_{slow} and the confinement size of nanodomain-
269 associated VGCCs were partially restored, with D_{slow} remaining slower than in WT, albeit short of
270 statistical significance ($p = 0.219$, Fig. 4b; Fig. S6c and S6d). This indicates that moderately
271 improved SV priming levels by UNC13S expression is sufficient to promote the mobility of slow
272 VGCCs, but that UNC13L-mediated priming is required to restore WT-level diffusion in AZ
273 nanodomains. VGCCs outside nanodomains were impacted in similar ways. D_{fast} decreased in *unc-*
274 *13(s69L-S-)* mutants, albeit short of statistical significance ($p = 0.178$), and it was only partially
275 restored to WT-levels in *unc-13(e51L-S+)* animals (Fig. 4c). Compared to WT, the channel
276 diffusion range became significantly smaller when both UNC-13 isoforms were ablated (*unc-13*$^{L-}$
277 $^{S-}$: 240 ± 23 nm *vs.* WT: 289 ± 29 nm) but it was restored by the sole expression of UNC-13S (*unc-*
278 *13*$^{L-S+}$: 310 ± 28 nm *vs.* WT: 289 ± 29 nm; Fig. 4c). Together, these results indicate that UNC-13-
279 mediated SV priming modulates the mobility of VGCCs both within and outside nanodomains at
280 the AZ.
281 To investigate if the structural organization of VGCCs at AZs was also modulated by UNC-13-
282 mediated SV priming, we imaged VGCCs and UNC-10 by STED in the two *unc-13* mutants. For
283 both VGCCs and UNC-10, the number of nanodomains per AZ and the size of nanodomains were

284 significantly lower in *unc-13(s69L-S-)* mutants compared to WT (Fig. 4d-4f; Fig. S6f), with the
285 distribution of UNC-10 nanodomains being more compact, but that of VGCC nanodomains being
286 unchanged (NND, Fig. S6e). The mean AZ puncta size of VGCCs and UNC-10 were both
287 significantly reduced (AED, Fig. 4g), indicating that AZs were globally smaller when UNC-13
288 mediated SV priming was abolished, which led to a decrease in the diffusion range of fast VGCCs.
289 With the expression of UNC-13S in *unc-13(e51L-S+)* mutants, VGCC nanodomain numbers, their
290 size and the AZ puncta sizes were only partially restored compared to WT animals (Fig. 4d-4g;
291 Fig. S6f). This indicates that UNC-13S-mediated SV priming influences the spatial distribution of
292 VGCCs, but that UNC-13L-mediated priming is required to maintain a WT structural organization
293 of the channels at AZs, consistent with our diffusion measurements. For UNC-10, the sole
294 expression of UNC-13S fully restored the number of nanodomains per AZ and their NND to WT
295 levels (Fig. 4e; Fig. S6e). Yet, in the absence of UNC-13L, the nanodomain size of UNC-10 and
296 its AZ puncta size remained well below WT levels and non-significantly different from *unc-*
297 *13(s69L-S-)* mutants (Fig. 4f and 4g). These results indicate that the number and distribution of
298 UNC-10 nanodomains are also modulated by UNC-13S-mediated SV priming, while UNC13-L
299 mediated priming contributes to the size of individual UNC-10 nanodomains and that of the AZ.
300 Surprisingly, the apparent rescue of VGCC nanodomain confinement and AZ diffusion range to
301 WT levels in *unc-13(e51L-S+)* animals (Fig. 4c) did not fully correlate with the nanodomain and
302 AZ puncta sizes for UNC-10 in those mutants (Fig. 4g), suggesting that, in the absence of UNC-
303 13L, UNC-13S-mediated SV priming induces VGCCs to diffuse beyond spatial boundaries
304 defined by UNC-10.
305 We next investigated whether the mobility of VGCCs is modulated by SNARE complex assembly
306 during SV priming and whether SV coupling, at this molecular step, impacts the channels diffusion.
307 We utilized the transgenic expression of the botulinum neurotoxin serotype B light chain protease
308 (ScBoNTB), which blocks full SNARE complex assembly by cleaving the v-SNARE vesicular
309 SNB-1[52]. As previously reported, expressing ScBoNTB in GABAergic neurons silenced inhibitory
310 neurotransmissions[52] and 92% of transgenic animals showed "shrinker" phenotypes (Fig.4h). For
311 proper comparison, we first reanalyzed the mobility of VGCCs specifically at GABAergic
312 synapses in WT animals by selecting trajectories only located at the tip of GABAergic boutons
313 (Fig. S6g). GABAergic VGCCs also exhibited two diffusive behaviors, with respective fractions
314 and diffusion coefficients that were non-significantly different from those observed across all

315 buttons, although D_{fast} appeared slightly faster (Fig. 4i and 4j; Fig. S6h). Only the confinement
316 size of nanodomain-associated GABAergic VGCCs was smaller ($WT^{GABAergic}$: 90 ± 25 nm *vs.*
317 WT^{All}: 104 ± 23 nm) (Fig. 4i). We then tracked GABAergic VGCCs in ScBoNTB-expressing
318 animals. We found that both D_{slow} and D_{fast} significantly decreased, an indication that the mobility
319 of VGCCs inside and outside AZ nanodomains is indeed modulated by a molecular priming of
320 SVs that requires full SNARE assembly (Fig. 4i and 4j; Fig. S6i). The diffusion range of VGCCs
321 outside nanodomains was also significantly reduced ($ScBoNTB^{GABAergic}$: 207 ± 29 nm *vs.*
322 $WT^{GABAergic}$: 278 ± 42 nm; Fig. 4j). But the confinement size of nanodomain-associated VGCCs
323 was unchanged compared to GABAergic WT (Fig. 4i), suggesting that it is independent of SNARE
324 complex assembly. Altogether, these results demonstrate that, downstream of UNC-10 mediated
325 channel-vesicle coupling and as part of UNC-13 mediated priming, the complete assembly of
326 SNARE complexes that clamp SVs is a critical step that modulates VGCC diffusions at AZs.
327

328 **The two mobilities of VGCCs are differentially modulated by UNC-13 isoforms and synaptic**
329 **vesicle priming levels**

330 We then examined if the mobility of VGCCs would positively scale with SV priming levels by
331 tuning the balance between UNC-13 isoforms and the t-SNAREs inhibitor TOM-1/Tomosyn. In
332 *C. elegans*, removal of TOM-1 markedly upregulates the pool of primed SVs throughout synaptic
333 terminals[53,54], and also partially rescues synaptic release defects in *unc-13* mutants[51]. We therefore
334 compared the diffusion of VGCCs in *tom-1;unc-13*$^{L\text{-}S\text{-}}$ versus *tom-1;unc-13*$^{L\text{-}S+}$ double mutants,
335 where SV priming levels are progressively restored, and in *tom-1(nu468)* single mutants where
336 priming levels are largely augmented[51,54]. As previously reported, both double mutants exhibited
337 significantly improved locomotion and neurotransmissions compared to the corresponding *unc-13*
338 single mutants, with SV release rescue being stronger in the presence of UNC-13S (Fig. 5a; Fig.
339 S7a). We found that D_{slow} for nanodomain-associated VGCCs was partially restored in *tom-1;unc-*
340 *13* $^{L\text{-}S\text{-}}$ animals, while their confinement size fully recovered to WT-level (*tom-1;unc-13*$^{L\text{-}S\text{-}}$: 111 ±
341 22 nm *vs.* WT: 104 ± 23 nm, Fig.5b), confirming that slow-diffusing VGCCs are modulated by
342 SV priming. However, despite enhanced SV priming levels, the mobility of VGCCs inside
343 nanodomains was not further improved by the expression of UNC-13S in *tom-1;unc-13*$^{L\text{-}S+}$ double
344 mutants, as it remained similar to *tom-1;unc-13*$^{L\text{-}S\text{-}}$ animals and to *unc-13(e51L-S+)* single mutants
345 (Fig. 5b; Fig. S7b-S7f). These results suggest that UNC-13S and TOM-1 have limited effect on

346 the mobility of nanodomain-associated VGCCs, which are primarily regulated by UNC-13L.
347 Indeed, the mobility of VGCCs in nanodomains did not further increase with augmented SV
348 priming levels in *tom-1(nu468)* single mutants (Fig. 5a and 5b; Fig. S7e).
349 On the contrary, for VGCCs outside nanodomains, both D_{fast} and their diffusion range significantly
350 increased in *tom-1(nu468)* animals (*tom-1*: 331 ± 33 nm *vs.* WT: 289 ± 29 nm; Fig. 5c). This
351 enhanced mobility was suppressed when UNC-13 was ablated in *tom-1;unc-13*$^{L-S-}$ double mutants,
352 where D_{fast} was similar to that in *unc-13(s69L-S-)* single mutants (Fig. 5c). However, the increase
353 in D_{fast} was largely preserved by UNC-13S expression in *tom-1;unc-13*$^{L-S+}$ double mutants, who
354 displayed significantly faster VGCC diffusion than in *tom-1;unc-13*$^{L-S-}$ animals (Fig. 5c; Fig. S7d-
355 S7f). This indicates that the faster mobility of VGCCs outside nanodomains in *tom-1(nu468)*
356 mutants is primarily UNC-13S-dependent, conforming with a previously reported upregulation of
357 UNC-13S abundance in these animals[54]. Together, these findings show that the mobility of VGCCs
358 is predominantly governed by UNC-13L-mediated SV priming inside nanodomains, and that it
359 scales with a pool of TOM-1 regulated and UNC-13S-primed SVs across the rest of the AZ.
360 Interestingly, the diffusion range of VGCCs outside nanodomains was dramatically expanded in
361 *tom-1;unc-13*$^{L-S-}$ double mutants (*tom-1;unc-13*$^{L-S-}$: 632 ± 112 nm *vs.* WT: 289 ± 29 nm; Fig. 5c),
362 in stark contrast with the reduction observed in *unc-13(s69L-S-)* single mutants. As the number of
363 membrane-contacting SVs located at the AZ periphery (400-600 nm away from the DPs)
364 substantially increases in *tom-1;unc-13*$^{L-S-}$ animals[53], our observation suggests that VGCCs can
365 diffuse far across the synaptic area where UNC-13-independent SV priming is upregulated.
366 Concurrently, in the same *tom-1;unc-13*$^{L-S-}$ animals, the size of UNC-10 puncta was significantly
367 reduced (Fig. 5e), indicating that, in the absence of UNC-13, the diffusion range of fast VGCCs is
368 set by the location of primed SVs rather than by the distribution of UNC-10 at AZ puncta. When
369 SV priming was controlled by UNC-13S in *tom-1;unc-13* $^{L-S+}$ double mutants, the diffusion range
370 of fast VGCCs was restored to WT levels (*tom-1;unc-13*$^{L-S+}$: 307 ± 37 nm *vs.* WT: 289 ± 29 nm),
371 together with the median puncta size of UNC-10 (Fig. 5c-5e). And when UNC-13S-mediated SV
372 priming was upregulated in *tom-1(nu468)* animals, this same diffusion range significantly
373 increased compared to WT (*tom-1*: 331 ± 33 nm *vs.* WT: 289 ± 29 nm; Fig. 5c), again exceeding
374 the median UNC-10 puncta size (Fig. 5c-5e). Together, these observations indicate that outside
375 nanodomains, the mobility of VGCCs is effectively governed by UNC-13S-mediated SV priming,

376 and that the channel diffusion range can expand when UNC-13-independent and spatially
377 imprecise SV priming is upregulated.
378 We also examined if increasing priming levels by TOM-1 removal modulates the AZ organization
379 of VGCC and UNC-10 nanodomains. We found that the defective nanodomain numbers and
380 puncta size of VGCCs we had observed when ablating the two UNC-13 isoforms were partially
381 restored by simultaneous removal of TOM-1 in *tom-1;unc-13*$^{L-S-}$ double mutants, although they
382 both remained significantly lower than WT (Fig. 5d-5f). The median number and NND of UNC-
383 10 nanodomains were back to WT-level, yet UNC-10 puncta sizes did not recover (Fig. 5d-5f; Fig.
384 S7g-S7i). These results are similar to those found in *unc-13(e51L-S+)* mutants, where SV priming
385 levels are improved and comparable to those of *tom-1;unc-13*$^{L-S-}$ animals[55]. Further improvements
386 of SV priming in *tom-1;unc-13* $^{L-S+}$ double mutants fully restored UNC-10 puncta sizes to WT
387 levels, but the organization of VGCC nanodomains remained partially defective (Fig. 5d-f),
388 confirming that UNC-13L is important for organizing VGCCs at the AZ. In *tom-1(nu468)* animals,
389 where both UNC-13 isoforms are present and UNC-13S-mediated priming is predominantly
390 upregulated, the spatial organizations of both VGCC and UNC-10 nanodomains were
391 indistinguishable from WT (Fig. 5d-5f). This suggests that VGCC and UNC-10 organizations scale
392 with SV priming levels up to a limit set by UNC-13L-activity. Collectively, these findings
393 demonstrate that UNC-13 mediated SV priming modulates the organization of VGCC and UNC-
394 10 nanodomains in a parallel and progressive manner. Notably the increase in UNC-10
395 nanodomain numbers is followed by an expansion of AZ puncta sizes, and the organization of
396 VGCC nanodomains exhibits greater sensitivity to priming levels than that of UNC-10.
397
398 **Primed synaptic vesicles can modulate the mobilities and multi-nanodomain organization of**
399 **VGCCs downstream of UNC-10**
400 As the diffusive behaviors of VGCCs are promoted by UNC-10 and SV priming, we tested whether
401 they both modulate VGCC mobility in the same molecular pathway by examining the channels
402 diffusion in *tom-1;unc-10* double mutants. Interestingly, the defective D_{slow} and confinement sizes
403 of nanodomain-associated VGCCs we observed in *unc-10(md1117)* single mutants were fully
404 restored to WT-level in *tom-1;unc-10* double mutants (Fig. 6a; Fig. S8a). Likewise, the diffusion
405 coefficient of VGCCs outside nanodomains was also significantly increased, with D_{fast} being faster
406 than in WT, albeit short of significance ($p = 0.193$, Fig. 6b), and being slower than the augmented

407 D_{fast} observed in *tom-1(nu468) single* mutants. Thus, upregulating SV priming levels can partially
408 bypass the role of UNC-10 in modulating the mobility of VGCCs. The diffusion range of fast
409 VGCCs in *tom-1;unc-10* double mutants showed significant increase compared to WT (*unc-*
410 *10*;*tom-1*: 336 ± 27 nm *vs.* WT: 289 ± 29 nm; Fig. 6b; Fig. S8a), phenocopying changes observed
411 in *tom-1(nu468)* animals and confirming that the diffusion range is set by primed SVs
412 independently of UNC-10. Together, it demonstrates that UNC-10 functions to couple mobile
413 VGCCs to primed SVs, which can directly modulate the channel mobilities downstream of UNC-
414 10. TOM-1 removal also largely rescued the impaired neurotransmissions in *unc-10(md1117)*
415 background (Fig. 6c) as previously reported[55]. Since UNC-10 is not required for molecular
416 priming[17,56], the rescue of synaptic releases through TOM-1 ablation in double mutants likely
417 stems from the upregulated SV priming levels and the restored VGCC mobility, which might
418 compensate for reduced SV docking[43].
419 Finally, we examined whether increasing priming levels can rescue the defective organizations of
420 VGCC nanodomains in the absence of UNC-10. In *tom-1;unc-10* animals, the number of VGCC
421 nanodomains per puncta was slightly but significantly increased compared to *unc-10(md1117)*
422 single mutants, yet it remained largely reduced compared to WT (Fig. 6d and 6e). In contrast, the
423 NND between nanodomains was non-significantly different from that in *unc-10(md1117)* animals,
424 showing a more dispersed organization compared to WT (Fig. 6f). These results demonstrate that
425 the multi-nanodomain organization of VGCCs at AZ requires UNC-10 and indicate that SV
426 priming levels regulate the spatial distribution of VGCC nanodomains through UNC-10.
427
428 **Discussion**
429 Using single channel tracking and super-resolution imaging in *C. elegans*, we dissected how
430 mobile VGCCs are spatiotemporally aligned with synaptic vesicles for precise neurotransmission.
431 We discovered that individual N-type VGCCs adopt distinct mobilities determined by their spatial
432 distribution and the molecular machinery coupling them to readily releasable SVs. VGCCs
433 tethered to primed SVs via a tripartite UNC-10/RAB-3/UNC-13L complex diffuse slowly in
434 multiple sub-AZ nanodomains that align with UNC-10/RIM scaffolds, whereas VGCCs coupled
435 to UNC-13S-primed SVs move significantly faster across the larger AZ puncta. The spatially
436 correlated multi-nanodomain arrangement of VGCCs and UNC-10 closely resembles Cav2 and
437 RIM1/2 nanoclusters observed at rodent hippocampal synapses[50,57], consistent with nematode

438 synapses exhibiting a multi-release-site organization similar to mammals[58]. Heterogeneity in
439 nanodomain number and size across synapses further points to a modular intra-AZ organization
440 that may enable local tuning of synaptic strength. Together, this nanoscale organization and the
441 distinct diffusion regimes of VGCCs likely give rise to diverse channel-vesicle coupling modes
442 that shape SV release probability.
443 In this context, UNC-10 emerges as a key regulator of VGCC mobility and nanodomain
444 organization. We found that UNC-10 promotes VGCC diffusion by coupling channels to primed
445 SVs, and that priming levels modulate both channel dynamics and multi-nanodomain organization.
446 As an SV docking factor and a direct modulator of VGCCs, UNC-10/RIM drives channel
447 accumulation at AZs[7,9,45], stabilizing them and securing their coupling distances to vesicles[8,18,59].
448 Consistent with these functions, UNC-10 facilitates the accumulation and tight organization of
449 multiple VGCC nanodomains at AZs. However, VGCCs can form nanodomains independently of
450 UNC-10 and, counterintuitively, UNC-10 enhances channel mobility. Thus, rather than simply
451 stabilizing VGCCs, UNC-10 modulates channel dynamics and shapes their nanotopography. The
452 influence of UNC-10 on VGCC diffusion appears conserved across species, as $Ca_V2.1$ isoforms
453 harboring or lacking RIM1/2 binding motifs exhibit different mobilities at rodent hippocampal
454 synapses[23], and Cac/Ca_V2 displays similarly slower diffusion in the absence of RIM at *Drosophila*
455 NMJs[25].
456 Importantly, at *C. elegans* NMJs, VGCCs within sub-AZ nanodomains and across the broader AZ
457 exhibit two different mobility regimes that both arise from coupling to primed SVs but are
458 governed by distinct molecular mechanisms. To dissect these mechanisms, we altered vesicle
459 priming through UNC-13 isoforms, the t-SNARE inhibitor TOM-1, and SNARE complex
460 blockade, and found that channel dynamics depend on UNC-13-mediated vesicle priming
461 following full SNARE assembly and SV-plasma membrane bridging. Within nanodomains,
462 VGCC dynamics are primarily driven by SV priming mediated through UNC-10/RAB-3/UNC-
463 13L complexes, with additional contributions from the UNC-13S isoform. Outside nanodomains,
464 however, this tripartite complex does not regulate VGCC mobility but instead influences the
465 channel distribution across AZ. In this region, VGCC dynamics scale with pools of UNC-13S-
466 primed or UNC-13-independent SVs, which are physiologically inhibited by TOM-1. Accordingly,
467 blocking SNARE assembly with ScBoNTB significantly reduces both VGCC diffusion and
468 restricts their AZ distribution, whereas removal of TOM-1 partially restores defective channel

469 dynamics in the absence of UNC-13 or even UNC-10. Thus, UNC-10-mediated SV coupling
470 drives VGCC diffusion following SNARE assembly, while primed SVs can further modulate
471 VGCC behavior beyond UNC-10-dependent coupling. These findings establish a causal link
472 between SV priming levels and channel dynamics and may mechanistically explain why conditions
473 that impair priming and SNARE assembly, such as intracellular Ca^{2+} chelation or silencing of
474 synaptic activity, are associated with reduced VGCC mobility but increased Syntaxin-1A/t-
475 SNARE diffusion[23,24,60].
476 Accordingly, the AZ distribution of fast VGCCs is primarily dictated by the location of primed
477 SVs rather than the multi-nanodomain organization of UNC-10. This is evident when simultaneous
478 removal of UNC-13 and TOM-1 leads to an expansion of VGCC diffusion range toward distal AZ
479 regions, where UNC-13-independent SV priming is upregulated[53]. The modest expansion
480 observed after disrupting UNC-10/UNC-13L interactions likely reflects a broadening in primed
481 SV distribution, with UNC-13L becoming less anchored at the AZ[55]. Conversely, removing RAB-
482 3 significantly reduces the diffusion range of VGCCs, as impaired SV docking limits their spatial
483 distribution across AZ. These observations indicate that VGCC topography is dynamically
484 instructed by the spatial distribution of primed SVs rather than solely imposed by AZ scaffolds.
485 Consistent with this relationship, SV priming levels progressively regulate the number and size of
486 VGCC and UNC-10 nanodomains, with the organization of VGCCs being more sensitive to
487 priming levels. These results complement previous findings that Ca_V2 clustering and vesicle
488 priming represent two distinct sub-assemblies tethered together by RIM[61]. Our data further
489 indicates that this tethering is itself regulated in a priming-level-dependent manner, with primed
490 vesicles reciprocally regulating UNC-10/RIM and directly shaping VGCC diffusion.
491 Collectively, our findings support a model in which primed SVs actively drive VGCC diffusion
492 through physical coupling, coordinating the movement of membrane-embedded channels with
493 that of adjacent primed SVs[62–66]. Such coordination likely secures the coupling distance between
494 the VGCC calcium donors and the SV-tethered synaptotagmin calcium sensors[1,67,68] thereby
495 ensuring precise neurotransmission within the highly dynamic environment of the AZ.
496 Furthermore, coupling distinct VGCC mobility to different pools of primed SVs suggests a level
497 of synaptic modularity that supports diverse release properties.
498 Placing this model in a broader context, studies at *Drosophila* and mammalian synapses[69–73],
499 together with functional analyses in *C. elegans* indicate that distinct channel-vesicle coupling

500 distances underlie different release properties, with fast release requiring UNC-13L and slow
501 release depending on both UNC-13L and UNC-13S[55,74]. Coupling distance has conventionally
502 been defined as the distance between docked SVs and the DP at the center of the AZ, where DP
503 markers appear as homogeneous puncta in diffraction-limited images[27,45,56]. Our studies reveal a
504 heterogeneous, multi-nanodomain topography of UNC-10 and VGCCs that closely resembles the
505 architecture of DP[42]. This spatial organization, together with differences in VGCC mobility and
506 their coupling to distinct UNC-13 isoforms, supports a multidimensional framework for generating
507 diverse SV release properties. Within this framework, UNC-13L-primed SVs preferentially dock
508 in nanodomains and tether slow-diffusing VGCCs, whose restricted mobility promotes
509 concentrated calcium influx[24] for fast release. In contrast, UNC-13S-primed SVs dock outside
510 nanodomains or at distal-AZ regions, where they couple to fast-diffusing VGCCs, whose higher
511 mobility yields more diffuse calcium influx for slow release. This framework further implies that
512 differences in channel mobility contribute to defining microdomain- and nanodomain-coupling
513 modes[20].
514 Whether and how primed SVs tether fast-diffusing VGCCs outside nanodomains remains unclear.
515 Because fast-diffusing VGCCs are not coupled to the tripartite UNC-10/RAB-3/UNC-13L
516 complex, the assembled SNARE complex itself may represent a candidate. While mammalian
517 Cav2 channels contain a "synprint" motif that directly binds SNARE complexes[4,75], UNC-2/Cav2
518 in *C. elegans* lacks such a sequence[76], and identifying the mechanisms that mediate coupling to
519 fast-diffusing VGCCs will require further investigation. Despite this evolutionary divergence, the
520 principle of vesicle-channel coupling may be more fundamental than the specific protein-protein
521 interactions that mediate it[77]. Another open question is what determines the transition between
522 slow and fast diffusion modes for VGCCs. It will be important to test whether coupled SV-VGCC
523 units move in and out of VGCC nanodomains together, potentially supporting transitions between
524 tightly primed (TS) and loosely primed (LS) states[78]. Addressing these questions will provide
525 further insight into how synapses exploit VGCC dynamics to achieve both reliability and plasticity.
526
527 In conclusion, this study identifies a mechanism by which presynaptic VGCC diffusion is actively
528 regulated by the release machinery and the priming status of SVs. The coupling of distinct channel
529 mobilities to different pools of primed vesicles reveals a previously unrecognized layer of AZ

530 organization that fine-tunes neurotransmitter release. Ultimately, this work establishes a
531 mechanistic framework to investigate the role of VGCC dynamics in synaptic function and disease.
532

533 **Acknowledgement**

534 We thank Dr. Dion Dickman and Dr. Kaikai He for providing important resource support and
535 advice for STED imaging and analysis. We thank Dr. Hong Zhan for advice on CALM imaging
536 and genome editing of *C. elegans*, and Dr. Carolyn Phillips for resource support on genetics. We
537 also thank Dr. Jean-Louis Bessereau for kindly sharing the unc-25p::snb-1::gfp strain, Dr. Peri
538 Kurshan for her kind gifts of GFP-UNC-2 related strains. We additionally thank Dr. Joshua Kaplan
539 for sharing tom-1(nu468) related strains, Dr. Alexander Gottschalk for kindly providing the unc-
540 47p::eGFP::ScBoNTB strain and Dr. Zhitao Hu for sharing the unc-10 (nu487 K77/79E) strain.
541 This work was funded by NIH grant NS114911 from the National Institute of Neurological
542 Disorders and Stroke (NINDS). YZ was partially supported by the NIGMS training grant
543 T32GM118289-04 Chemistry Biology Interface Training Grant at the University of Southern
544 California. Some strains were obtained from the Caenorhabditis Genetics Center (CGC) that is
545 funded by the NIH Office of Research Infrastructure Programs (P40 OD010440).
546
547

548 **Methods**

549 ***C. elegans* culture and maintenance**

550 All *Caenorhabditis elegans* nematode strains were raised on nematode growth media (NGM)
551 plates at 20°C and fed on OP50 *Escherichia coli* as previously described[33]. All *C. elegans* used for
552 experiments were adult hermaphrodites. Worms were handled using a Nikon dissecting
553 microscope (SM2745). A full list of strains is available in Supplementary Table 1.
554

555 **Molecular biology**

556 For genotyping, worms were lysed in worm lysis buffer as previously described[30]. Worm lysates
557 were amplified using either 2xTaq PCR Premix (Bioland) or Phusion High-fidelity DNA
558 Polymerase (NEB). For CRISPR-Cas9 genome editing, direct microinjection of *in vitro*–
559 assembled CRISPR-Cas9 and single chimeric guide RNA (sgRNA) ribonucleoprotein complexes
560 into the gonads of hermaphrodite worms were performed as previously described[30,79]. Cas9

561 endonuclease was expressed *in vitro* using DE3 GOLD (Agilent) cells transformed with the
562 nm2973 plasmid[80] and was prepared to 10 µg/µl. Single-stranded DNA oligonucleotides (ssODNs)
563 were ordered from Integrated DNA Technology (IDT). DNA templates for sgRNA combining
564 tracrRNA and crRNA were amplified from two complementary ssODNs. sgRNA were transcribed
565 *in vitro* using a MEGA shortscript T7 kit (Thermo Fisher Scientific) and prepared at 2 µg/µl. Linear
566 homology-dependent repair templates (HDRT) containing 35-nucleotide homology arms were
567 amplified using Phusion HF PCR reactions and were prepared at 1 µg/µl. The *dpy-10* co-CRISPR
568 approach[81], which generates a roller phenotype was used for screening progeny with high edit
569 frequency. A total 15 µl mix of ribonucleoprotein complexes containing Cas9 endonuclease,
570 sgRNA and HDRT for the targeted genes and *dpy-10* were incubated at 37 °C for 10 min and spun
571 at 13,000 rpm for 2 min before gonad microinjections. To generate the sCherry::unc-36 transgenic
572 strain, linear HDRT were amplified using plasmids pcDNA3.1-sfCherry2(1-10)[82] (Addgene) as
573 PCR templates. For generating 5xMYC::unc-10 and HA::unc-2 strains or mutating the marker
574 gene *dpy-10*, ssODNs (IDT) were used as the HDRT. A silent mutation for the fifth Serine of UNC-
575 10 was introduced in the HDRT to prevent Cas9 recognition. All generated worm lines were
576 outcrossed at least three times to remove potential off-target mutations. A full list of primers,
577 sgRNAs and HDRT is available in Supplementary Table 2.
578
579 **Microinjection**
580 Microinjection was performed as previously described[30]. For genome editing, standard gonad
581 microinjection was done on young adult worms. For CALM imaging, synthetic complementary
582 peptide sfCherry2(11)-cysteine (NH_2-C-acp-linker GSGGGSTSYTIVEQYERAEARHSTGG-
583 COOH, LifeTein, LLC.75% purity) was first dissolved in DMSO to as a 30mM stock, which was
584 then diluted to 750µM with PBS buffer right before microinjections. For immunostaining of
585 extracellular sCherry-UNC-36, rabbit anti-mCherry (Abcam Cat# ab167453, RRID: AB_2571870)
586 was freshly diluted at 1:400 with injection buffer[83] (20 mM K_2HPO_4, 3 mM potassium citrate, 2%
587 PEG3000, pH 7.4). Either peptide or antibody solutions were spun at 15,000 rpm for 2 min before
588 microinjection into the pseudocoelomic cavity at the head region of staged 1-day adult worms.
589 Animals were recovered in recover buffer (5 mM HEPES pH 7.2, 3 mM $CaCl_2$, 3 mM $MgCl_2$, 66
590 mM NaCl, 2.4 mM KCl, 4% w/v glucose) drop on a NGM plate at room temperature for 16-20 h
591 before imaging or freeze cracking. Microinjection was done with an inverted IX50 Olympus

592 microscope, equipped with an Eppendorf FemtoJet micro-injector connected to FemtotipII
593 microinjection capillaries held on a Leitz manual micromanipulator.
594
595 **Behavioral assays**
596 Aldicarb acute paralysis assays and body bending thrashing assays were performed on staged 1-
597 day adult worms as previously described[84,85]. Numbers of body bending per minute were scored
598 in the M9 buffer added to 35 mm sterile NGM agar plates. Worms were first accommodated in
599 M9 buffer for 2 min and the number of sinusoidal curves made within a 2 min period were counted.
600 At least 15 worms were scored for each strain. For aldicarb assays, 6-well NGM plates containing
601 1 mM aldicarb were made and seeded with OP50 bacteria the day before the assays. For each strain,
602 30 animals were placed on plates and monitored every 30 min for 4 h. Worms were considered
603 paralyzed if their whole body including nose and tail regions show no movement after a gentle tap
604 on the head using a worm pick. For comparison to mutant animals, wildtype control worms were
605 cultured and scored simultaneously on the same batch of NGM or aldicarb plates. At least three
606 trials, with independent worm cultures, were performed for each assay. Data collections were
607 performed blinded to the animal strains. Data were analyzed using either GraphPad Prism software
608 version 8.0.2(263) or OriginPro software version 10.1.0.178.
609
610 **Image acquisition for CALM**
611 CALM imaging was performed as previously described[30]. 16-20h post peptide microinjection,
612 worms were anesthetized for 6-10 min in M9 buffer containing 30 mg/mL 2,3-butanedione
613 monoxime (BDM, Sigma) in a 35 mm plate. Anesthetized worms were then mounted in 8 µL BDM
614 solution on freshly prepared 2% agarose pads with high-precision Deckglaser microscope
615 coverslips (Marienfeld, 0117650). Worms were positioned with one of the nerve cords facing
616 upright by gentling sliding the coverslip without pressing down. The worm position was secured
617 by sealing the four quarters of the coverslip to the slide with minimal nail polish and stabilized for
618 10min before imaging. Anesthetized worms were imaged within 40 min, after which locomotion
619 recovered. Simultaneous dual-color imaging of Punc-25::SNB-1::GFP and sCherry-UNC-36 was
620 performed on an inverted Nikon Eclipse Ti-E microscope equipped with HiLO optics, a 100x 1.49
621 NA objective (Nikon), 488 and 561 nm fiber-coupled excitation lasers (Agilent), a multiband pass
622 ZET405/488/561/647 excitation filter (Chroma), a quad-band ZT405/488/561/647 dichroic mirror

623 (Chroma), two EMCCD cameras (Andor iXon), a dual-camera imaging adapter (Andor), an
624 emission-splitting FF560FDi01 dichroic mirror (Semrock), and emission filters at 525/50 nm
625 (Semrock) for GFP and 600/50 nm (Chroma) for sCherry imaging. Movies were acquired at a
626 frame rate of 80 ms/frame, with EMCCD gains of 300, and 1 x1 binning, leading to image pixel
627 sizes of 107 nm on each camera. Dual-channel alignment was done by imaging 40 nm diameter
628 TransFluoSphere beads (488/685, Invitrogen) at 1:10000 dilution. CALM imaging of individual
629 sCherry-UNC-36 was performed by continuous HiLO illumination of nerve cords marked by
630 either GFP-UNC-2 or Punc-25::SNB-1::GFP for 1-2 min per field of view from the tail to the head
631 regions of each animal. GFP channel was excited with minimal laser intensity to reduce
632 background. Single molecule detections of sCherry-UNC-36 showed typical blinking events,
633 single-step photobleaching, and sudden fluorescence appearance, as previously described[29,30].
634 Each strain condition was imaged with at least three independent cultures of worms. The numbers
635 of animals imaged for each strain are indicated in figure legends.
636
637 **Tracking and diffusion analyses**
638 Single molecule tracking was performed as previously described[29,30] using the Matlab software
639 SLIMfast, which is based on multiple-target tracing algorithms[86]. For sub-diffraction limit
640 localizations and trajectory assembly of sCherry-UNC-36, the following parameters were used for
641 all conditions: 107 nm/pixel, 80 ms/frame, 10^{-6} localization error, fixed PSF radius of 1.02 pixel
642 determined by theoretical calculation for a 1.49 NA and 615 nm maximum emission wavelength,
643 0.5-3 pixels search limit and maximum gap of 3 steps for linking positions. Only trajectories with
644 a minimal number of 3 steps were kept for diffusion analyses. Diffusion analyses of neuronal
645 VGCCs were performed on sCherry-UNC-36 trajectories located along the nerve cords or, in the
646 case of only GABAergic VGCCs, that overlapped with synaptic boutons marked by Punc-
647 25::SNB-1::GFP. For each strain condition, trajectories from multiple worms were pooled together
648 and analyzed using the PDSD method[30] to differentiate diffusive behaviors, and determine the
649 numbers, fractions and mean square displacements of each diffusion regime. Mean square
650 displacement curves for the first 10 steps were plotted for each behavior and fitted with a 2D
651 circularly confined diffusion model[29] to compute the diffusion coefficients and radius of
652 confinement. OriginPro software version 10.1.0.178 was used for data analysis.

653 **Immunofluorescence staining for confocal and STED microscopy**

654 Worms were harvested at stage 2-day adult or 18h post antibody microinjection for
655 immunostaining of extracellular sCherry-UNC-36. Worms were mounted on slides with ice cold
656 Milli-Q water and frozen on dry ice for 1 hour before freeze-cracking as previously described[87].
657 Fixation was done overnight at 4 °C in microcentrifuge tubes with phosphate-buffered saline (PBS)
658 containing 1% paraformaldehyde (PFA). For HA-UNC-2 immunostaining, fixation was reduced
659 to 20 min at room temperature. Fixation was followed by three 20 min washes with PBS at 4 °C
660 and blocking in blocking solution (PBS, 5% BSA, 0.5% Triton X-100, 1mM EDTA pH 8, 0.05%
661 Sodium azide) for 1 h at room temperature or overnight at 4 °C. Incubations with primary and
662 secondary antibodies were each done overnight at 4 °C in antibody solution (PBS, 2.5% BSA, 0.5%
663 Triton X-100, 1mM EDTA pH 8, 0.05% Sodium azide). Three 20 min washes with PBST (0.5%
664 Tween) were performed at 4 °C between each incubation and one 5 min final wash with PBS was
665 done before mounting. Samples were mounted using high-precision Deckglaser coverslips
666 (Marienfeld, 0117650) and ProLong Glass Antifade Mountant (Invitrogen). Mounted samples
667 were cured for 24 h at room temperature before imaging. The primary antibodies used were rabbit
668 anti-mCherry (Abcam Cat# ab167453, RRID: AB_2571870; 1:400), mouse anti-MYC (Cell
669 Signaling Technology Cat# 2276, RRID: AB_331783; 1:1000), rat anti-HA (Roche Cat#
670 11867423001, RRID: AB_390918; 1: 100) and chicken anti-GFP (Aves Labs Cat# GFP-1010,
671 RRID: AB_2307313; 1:200). The secondary antibodies used were goat anti-rabbit STAR RED
672 (Abberior Cat# STRED-1002-500UG, RRID: AB_2833015; 1:400), goat anti-mouse STAR RED
673 (Abberior Cat# STRED-1001-500UG, RRID: AB_3068620; 1:600), goat anti-mouse Alexa Fluor
674 594 (Jackson Immuno Research Labs Cat# 115-585-146, RRID: AB_2338881; 1:500), goat anti-
675 rat Alexa Fluor 594 (Thermo Fisher Scientific Cat# A-11007, RRID:AB_10561522; 1:200) and
676 goat anti-chicken IgY Alexa Fluor 594 (Thermo Fisher Scientific Cat# A-11042,
677 RRID:AB_2534099; 1:500).

678

679 **Image acquisition and analyses for confocal and STED microscopy**

680 Both confocal and STED imaging were performed on a Nikon Eclipse FN1 upright microscope
681 equipped with an Abberior STEDYCON system, four excitation lasers (640, 561, 488, and 405
682 nm), a pulsed STED laser of 775 nm, and three avalanche photodiode detectors operating in single
683 photon counting mode. 2D STED images were acquired using a 100× Nikon Plan APO 1.45 NA

684 oil immersion objective, fixed pixel size of 15 nm, a dwell time set at 10 µs, 5x line accumulation
685 in photon counting mode, and time gating set at 1 ns with a 6 ns width for all channels. Dual-color
686 STED images were acquired using 775 nm depletion beam with the same depletion power for both
687 STAR RED and Alexa Fluor 594 fluorophores. Confocal scans with 1x line accumulation for all
688 channels were done before STED scans, using 5x line accumulation for the same channels. To
689 overlay STED and confocal images of Punc-25::SNB-1::GFP, 5x line accumulation was also used.
690 Acquisition settings for each channel were identical in all conditions. Imaging field of views with
691 sizes of 10 µm or 20 µm x 3µm were used. 5-15 different animals were imaged for each condition.
692 Only dorsal nerve cords were imaged as cell bodies often interfered with imaging at ventral nerve
693 cords.
694 For figures display, raw STED images were deconvolved with the Huygens Essential version 24.10
695 software (Scientific Volume Imaging, The Netherlands, http://svi.nl) using the standard mode and
696 theoretical point spread functions of the STED microscope. For quantitative analysis of UNC-36
697 and UNC-10, raw images were processed with the Savitzky Golay denoise filter[88] of the Space
698 Noise Reduce plugin in ImageJ/Fiji, setting the parameter order at 7 and the width at 5.
699 Segmentations and measurements of puncta and nanodomains were done with the Particle Sizer
700 plugin[89] in ImageJ/Fiji, using the single particle mode for puncta and the watershed mode for
701 irregular structures mode for nanodomain. AZs with planar orientation where both UNC-36 and
702 UNC-10 signals could be clearly resolved were manually selected for measurements.
703 Segmentations parameters were optimized using both WT animals and mutants with severe
704 phenotypes and were kept identical for each protein and all conditions. The number of
705 nanodomains and their nearest neighborhood distance (NND) were quantified by treating each
706 nanodomain as a theoretical point spread function to localize its center position. The images were
707 first processed with the Rolling Ball Background Subtraction algorithm[90] built in ImageJ/Fiji,
708 using with a 10-pixel rolling ball radius, and center localizations and NND measurements were
709 done in the Picasso software[91]. The same settings were used for all conditions. All measurements
710 were done on 2D STED images taken from staged 2-day adult worms. Data analysis and statistics
711 were performed using OriginPro software version 10.1.0.178.
712
713

714 **References**

715 1. Emperador-Melero, J. & Kaeser, P. S. Assembly of the presynaptic active zone. *Curr. Opin.*
716 *Neurobiol.* **63**, 95–103 (2020).

717 2. Katz, B. Quantal Mechanism of Neural Transmitter Release. *Science* **173**, 123–126 (1971).

718 3. Südhof, T. C. Neurotransmitter Release: The Last Millisecond in the Life of a Synaptic Vesicle.
719 *Neuron* **80**, 675–690 (2013).

720 4. Dolphin, A. C. & Lee, A. Presynaptic calcium channels: specialized control of synaptic
721 neurotransmitter release. *Nat. Rev. Neurosci.* **21**, 213–229 (2020).

722 5. Nanou, E. & Catterall, W. A. Calcium channels, synaptic plasticity, and neuropsychiatric
723 disease. *Neuron* **98**, 466–481 (2018).

724 6. Jánosi, B. *et al.* RIM and RIM-Binding Protein Localize Synaptic CaV2 Channels to
725 Differentially Regulate Transmission in Neuronal Circuits. *J. Neurosci.* **44**, e0535222024
726 (2024).

727 7. Kaeser, P. S. *et al.* RIM Proteins Tether Ca2+ Channels to Presynaptic Active Zones via a
728 Direct PDZ-Domain Interaction. *Cell* **144**, 282–295 (2011).

729 8. Koushika, S. P. *et al.* A post-docking role for active zone protein Rim. *Nat. Neurosci.* **4**, 997–
730 1005 (2001).

731 9. Kushibiki, Y., Suzuki, T., Jin, Y. & Taru, H. RIMB-1/RIM-Binding Protein and UNC-10/RIM
732 Redundantly Regulate Presynaptic Localization of the Voltage-Gated Calcium Channel in
733 *Caenorhabditis elegans*. *J. Neurosci.* **39**, 8617–8631 (2019).

734 10. Betz, A. *et al.* Functional Interaction of the Active Zone Proteins Munc13-1 and RIM1 in
735 Synaptic Vesicle Priming. *Neuron* **30**, 183–196 (2001).

736 11. Deng, L., Kaeser, P. S., Xu, W. & Südhof, T. C. RIM Proteins Activate Vesicle Priming by
737 Reversing Autoinhibitory Homodimerization of Munc13. *Neuron* **69**, 317–331 (2011).

738 12. Dulubova, I. *et al.* A Munc13/RIM/Rab3 tripartite complex: from priming to plasticity? *EMBO*
739 *J.* **24**, 2839–2850 (2005).

740 13. Rizo, J. Molecular Mechanisms Underlying Neurotransmitter Release. *Annu. Rev. Biophys.* **51**,
741 377–408 (2022).

742 14. Jahn, R. & Scheller, R. H. SNAREs — engines for membrane fusion. *Nat. Rev. Mol. Cell Biol.*
743 **7**, 631–643 (2006).

744 15. Richmond, J. E., Weimer, R. M. & Jorgensen, E. M. An open form of syntaxin bypasses the
745 requirement for UNC-13 in vesicle priming. *Nature* **412**, 338–341 (2001).

746 16. Südhof, T. C. & Rothman, J. E. Membrane Fusion: Grappling with SNARE and SM Proteins.
747 *Science* **323**, 474–477 (2009).

748 17. Liu, H. *et al.* Heterodimerization of UNC-13/RIM regulates synaptic vesicle release
749 probability but not priming in C. elegans. *eLife* **8**, e40585 (2019).

750 18. Dittman, J. S. & Ryan, T. A. The control of release probability at nerve terminals. *Nat. Rev.*
751 *Neurosci.* **20**, 177–186 (2019).

752 19. Nakamura, Y. *et al.* Nanoscale Distribution of Presynaptic Ca2+ Channels and Its Impact on
753 Vesicular Release during Development. *Neuron* **85**, 145–158 (2015).

754 20. Eggermann, E., Bucurenciu, I., Goswami, S. P. & Jonas, P. Nanodomain coupling between
755 Ca2+ channels and sensors of exocytosis at fast mammalian synapses. *Nat. Rev. Neurosci.* **13**,
756 7–21 (2012).

757 21. Guerrier, C. & Holcman, D. The First 100 nm Inside the Pre-synaptic Terminal Where Calcium
758 Diffusion Triggers Vesicular Release. *Front. Synaptic Neurosci.* **10**, 23 (2018).

759 22. Mercer, A. J., Chen, M. & Thoreson, W. B. Lateral mobility of presynaptic L-type calcium
760 channels at photoreceptor ribbon synapses. *J. Neurosci.* **31**, 4397–4406 (2011).

761 23. Heck, J. *et al.* Transient Confinement of CaV2.1 Ca2+-Channel Splice Variants Shapes
762 Synaptic Short-Term Plasticity. *Neuron* **103**, 66-79.e12 (2019).

763 24. Schneider, R. *et al.* Mobility of calcium channels in the presynaptic membrane. *Neuron* **86**,
764 672–679 (2015).

765 25. Ghelani, T. *et al.* Interactive nanocluster compaction of the ELKS scaffold and Cacophony
766 Ca^{2+} channels drives sustained active zone potentiation. *Sci. Adv.* **9**, eade7804 (2023).

767 26. Tong, X.-J. *et al.* Retrograde Synaptic Inhibition Is Mediated by α-Neurexin Binding to the
768 α2δ Subunits of N-Type Calcium Channels. *Neuron* **95**, 326-340.e5 (2017).

769 27. Oh, K. H., Xiong, A., Choe, J., Richmond, J. E. & Kim, H. Active Zone Trafficking of
770 CaV2/UNC-2 Channels Is Independent of β/CCB-1 and α2δ/UNC-36 Subunits. *J. Neurosci.*
771 **43**, 5142–5157 (2023).

772 28. Saheki, Y. & Bargmann, C. I. Presynaptic CaV2 calcium channel traffic requires CALF-1 and
773 the α2δ subunit UNC-36. *Nat. Neurosci.* **12**, 1257–1265 (2009).

774 29. Zhan, H. *et al.* In vivo single-molecule imaging identifies altered dynamics of calcium
775 channels in dystrophin-mutant C. elegans. *Nat. Commun.* **5**, 4974 (2014).

776 30. Zhao, Y. & Pinaud, F. In Vivo Single-Molecule Tracking of Voltage-Gated Calcium Channels
777 with Split-Fluorescent Proteins in CRISPR-Engineered C. elegans. in *Single Molecule*
778 *Microscopy in Neurobiology* (eds Yamamoto, N. & Okada, Y.) vol. 154 11–37 (Springer US,
779 New York, NY, 2020).

780 31. Feng, S. *et al.* Improved split fluorescent proteins for endogenous protein labeling. *Nat.*
781 *Commun.* **8**, 370 (2017).

782 32. Tzur, Y. B. *et al.* Heritable custom genomic modifications in Caenorhabditis elegans via a
783 CRISPR-Cas9 system. *Genetics* **195**, 1181–1185 (2013).

784 33. Brenner, S. THE GENETICS OF *CAENORHABDITIS ELEGANS*. *Genetics* **77**, 71–94 (1974).

785 34. Laine, V., Frokjaer-Jensen, C., Couchoux, H. & Jospin, M. The alpha1 subunit EGL-19, the
786 alpha2/delta subunit UNC-36, and the beta subunit CCB-1 underlie voltage-dependent calcium
787 currents in Caenorhabditis elegans striated muscle. *J. Biol. Chem.* **286**, 36180–36187 (2011).

788 35. McDonald, K. *et al.* Using CRISPR knock-in of fluorescent tags to examine isoform-specific
789 expression of EGL-19 in C. elegans.

https://doi.org/10.17912/MICROPUB.BIOLOGY.000858 (2023) doi:10.17912/MICROPUB.BIOLOGY.000858.

36. Mueller, B. D. *et al.* CaV1 and CaV2 calcium channels mediate the release of distinct pools of synaptic vesicles. *eLife* **12**, e81407 (2023).

37. Zhao, J., Gao, L., Nurrish, S. & Kaplan, J. M. Post-synaptic GABAA receptors potentiate transmission by recruiting CaV2 channels to their inputs. *Cell Rep.* **42**, 113161 (2023).

38. Serge, A., Bertaux, N., Rigneault, H. & Marguet, D. Dynamic multiple-target tracing to probe spatiotemporal cartography of cell membranes. *Nat. Methods* **5**, 687–694 (2008).

39. Schutz, G. J., Schindler, H. & Schmidt, T. Single-molecule microscopy on model membranes reveals anomalous diffusion. *Biophys. J.* **73**, 1073–1080 (1997).

40. Watanabe, S. *et al.* Ultrafast endocytosis at Caenorhabditis elegans neuromuscular junctions. *eLife* **2**, e00723 (2013).

41. Ackermann, F., Waites, C. L. & Garner, C. C. Presynaptic active zones in invertebrates and vertebrates. *EMBO Rep.* **16**, 923–938 (2015).

42. Kittelmann, M. *et al.* Liprin-α/SYD-2 determines the size of dense projections in presynaptic active zones in *C. elegans*. *J. Cell Biol.* **203**, 849–863 (2013).

43. Stigloher, C., Zhan, H., Zhen, M., Richmond, J. & Bessereau, J.-L. The Presynaptic Dense Projection of the *Caenorhabiditis elegans* Cholinergic Neuromuscular Junction Localizes Synaptic Vesicles at the Active Zone through SYD-2/Liprin and UNC-10/RIM-Dependent Interactions. *J. Neurosci.* **31**, 4388–4396 (2011).

44. Calahorro, F. & Izquierdo, P. G. The presynaptic machinery at the synapse of C. elegans. *Invert. Neurosci.* **18**, 4 (2018).

45. Oh, K. H., Krout, M. D., Richmond, J. E. & Kim, H. UNC-2 CaV2 Channel Localization at Presynaptic Active Zones Depends on UNC-10/RIM and SYD-2/Liprin-α in *Caenorhabditis elegans*. *J. Neurosci.* **41**, 4782–4794 (2021).

46. Nonet, M. L. *et al. Caenorhabditis elegans rab-3* Mutant Synapses Exhibit Impaired Function and Are Partially Depleted of Vesicles. *J. Neurosci.* **17**, 8061–8073 (1997).

47. Weimer, R. M. *et al.* UNC-13 and UNC-10/Rim Localize Synaptic Vesicles to Specific Membrane Domains. *J. Neurosci.* **26**, 8040–8047 (2006).

48. Gracheva, E. O., Hadwiger, G., Nonet, M. L. & Richmond, J. E. Direct interactions between C. elegans RAB-3 and Rim provide a mechanism to target vesicles to the presynaptic density. *Neurosci. Lett.* **444**, 137–142 (2008).

49. Dittman, J. S. Unc13: a multifunctional synaptic marvel. *Curr. Opin. Neurobiol.* **57**, 17–25 (2019).

50. Sakamoto, H. Synaptic weight set by Munc13-1 supramolecular assemblies. *Nat Neurosci* **21**, (2018).

51. Hu, Z., Tong, X.-J. & Kaplan, J. M. UNC-13L, UNC-13S, and Tomosyn form a protein code for fast and slow neurotransmitter release in Caenorhabditis elegans. *eLife* **2**, e00967 (2013).

52. Liu, Q. *et al.* A Photoactivatable Botulinum Neurotoxin for Inducible Control of Neurotransmission. *Neuron* **101**, 863-875.e6 (2019).

53. Gracheva, E. O. *et al.* Tomosyn Inhibits Synaptic Vesicle Priming in Caenorhabditis elegans. *PLoS Biol.* **4**, e261 (2006).

54. McEwen, J. M., Madison, J. M., Dybbs, M. & Kaplan, J. M. Antagonistic Regulation of Synaptic Vesicle Priming by Tomosyn and UNC-13. *Neuron* **51**, 303–315 (2006).

55. Hu, Z., Tong, X.-J. & Kaplan, J. M. UNC-13L, UNC-13S, and Tomosyn form a protein code for fast and slow neurotransmitter release in Caenorhabditis elegans. *eLife* **2**, e00967 (2013).

56. Krout, M. *et al. C. elegans* Clarinet/CLA-1 recruits RIMB-1/RIM-binding protein and UNC-13 to orchestrate presynaptic neurotransmitter release. *Proc. Natl. Acad. Sci.* **120**, e2220856120 (2023).

57. Sakamoto, H. *et al.* Synapse type-specific molecular nanoconfigurations of the presynaptic active zone in the hippocampus identified by systematic nanoscopy. Preprint at https://doi.org/10.1101/2022.03.11.483942 (2022).

58. Maschi, D. & Klyachko, V. A. Spatiotemporal Regulation of Synaptic Vesicle Fusion Sites in Central Synapses. *Neuron* **94**, 65-73.e3 (2017).

59. Südhof, T. C. The presynaptic active zone. *Neuron* **75**, 11–25 (2012).

60. Bademosi, A. T. *et al.* In vivo single-molecule imaging of syntaxin1A reveals polyphosphoinositide- and activity-dependent trapping in presynaptic nanoclusters. *Nat. Commun.* **7**, 13660 (2016).

61. Emperador-Melero, J. *et al.* Distinct active zone protein machineries mediate Ca2+ channel clustering and vesicle priming at hippocampal synapses. *Nat. Neurosci.* **27**, 1680–1694 (2024).

62. Gaffield, M. A., Rizzoli, S. O. & Betz, W. J. Mobility of Synaptic Vesicles in Different Pools in Resting and Stimulated Frog Motor Nerve Terminals. *Neuron* **51**, 317–325 (2006).

63. Park, H., Li, Y. & Tsien, R. W. Influence of Synaptic Vesicle Position on Release Probability and Exocytotic Fusion Mode. *Science* **335**, 1362–1366 (2012).

64. Forte, L. A., Gramlich, M. W. & Klyachko, V. A. Activity-Dependence of Synaptic Vesicle Dynamics. *J. Neurosci.* **37**, 10597–10610 (2017).

65. Shtrahman, M., Yeung, C., Nauen, D. W., Bi, G. & Wu, X. Probing Vesicle Dynamics in Single Hippocampal Synapses. *Biophys. J.* **89**, 3615–3627 (2005).

66. Miki, T., Midorikawa, M. & Sakaba, T. Direct imaging of rapid tethering of synaptic vesicles accompanying exocytosis at a fast central synapse. *Proc. Natl. Acad. Sci.* **117**, 14493–14502 (2020).

67. Südhof, T. C. The presynaptic active zone. *Neuron* **75**, 11–25 (2012).

68. Kobbersmed, J. R., Berns, M. M., Ditlevsen, S., Sørensen, J. B. & Walter, A. M. Allosteric stabilization of calcium and phosphoinositide dual binding engages several synaptotagmins in fast exocytosis. *eLife* **11**, e74810 (2022).

69. Bohme, M. A. Active zone scaffolds differentially accumulate Unc13 isoforms to tune Ca2+ channel-vesicle coupling. *Nat Neurosci* **19**, (2016).

867 70. Nakamura, Y. *et al.* Nanoscale Distribution of Presynaptic Ca2+ Channels and Its Impact on
868 Vesicular Release during Development. *Neuron* **85**, 145–158 (2015).

869 71. Rebola, N. *et al.* Distinct Nanoscale Calcium Channel and Synaptic Vesicle Topographies
870 Contribute to the Diversity of Synaptic Function. *Neuron* **104**, 693-710.e9 (2019).

871 72. Vyleta, N. P. & Jonas, P. Loose Coupling Between Ca^{2+} Channels and Release Sensors at a
872 Plastic Hippocampal Synapse. *Science* **343**, 665–670 (2014).

873 73. Reddy-Alla, S. Stable positioning of Unc13 restricts synaptic vesicle fusion to defined release
874 sites to promote synchronous neurotransmission. *Neuron* **95**, (2017).

875 74. Zhou, K., Stawicki, T. M., Goncharov, A. & Jin, Y. Position of UNC-13 in the active zone
876 regulates synaptic vesicle release probability and release kinetics. *eLife* **2**, e01180 (2013).

877 75. Zamponi, G. W. Regulation of Presynaptic Calcium Channels by Synaptic Proteins. *J.*
878 *Pharmacol. Sci.* **92**, 79–83 (2003).

879 76. Mathews, E. A. *et al.* Critical Residues of the *Caenorhabditis elegans unc-2* Voltage-Gated
880 Calcium Channel That Affect Behavioral and Physiological Properties. *J. Neurosci.* **23**, 6537–
881 6545 (2003).

882 77. Tan, C., Wang, S. S. H., De Nola, G. & Kaeser, P. S. Rebuilding essential active zone functions
883 within a synapse. *Neuron* **110**, 1498-1515.e8 (2022).

884 78. Neher, E. & Brose, N. Dynamically Primed Synaptic Vesicle States: Key to Understand
885 Synaptic Short-Term Plasticity. *Neuron* **100**, 1283–1291 (2018).

886 79. Paix, A., Folkmann, A. & Seydoux, G. Precision genome editing using CRISPR-Cas9 and
887 linear repair templates in C. elegans. *Methods* **121–122**, 86–93 (2017).

888 80. Hua Fu, B. X., Hansen, L. L., Artiles, K. L., Nonet, M. L. & Fire, A. Z. Landscape of
889 target:guide homology effects on Cas9-mediated cleavage. *Nucleic Acids Res.* **42**, 13778–
890 13787 (2014).

891 81. Arribere, J. A. *et al.* Efficient Marker-Free Recovery of Custom Genetic Modifications with
892 CRISPR/Cas9 in *Caenorhabditis elegans*. *Genetics* **198**, 837–846 (2014).

893 82. Feng, S. *et al.* Improved split fluorescent proteins for endogenous protein labeling. *Nat.*
894 *Commun.* **8**, 370 (2017).

895 83. Gottschalk, A. & Schafer, W. R. Visualization of integral and peripheral cell surface proteins
896 in live Caenorhabditis elegans. *J. Neurosci. Methods* **154**, 68–79 (2006).

897 84. Mahoney, T. R., Luo, S. & Nonet, M. L. Analysis of synaptic transmission in Caenorhabditis
898 elegans using an aldicarb-sensitivity assay. *Nat. Protoc.* **1**, 1772–1777 (2006).

899 85. Nawa, M. & Matsuoka, M. The Method of the Body Bending Assay Using Caenorhabditis
900 elegans. *BIO-Protoc.* **2**, (2012).

901 86. Sergé, A., Bertaux, N., Rigneault, H. & Marguet, D. Dynamic multiple-target tracing to probe
902 spatiotemporal cartography of cell membranes. *Nat. Methods* **5**, 687–694 (2008).

903 87.Duerr, J. Immunohistochemistry. *WormBook* https://doi.org/10.1895/wormbook.1.105.1 (2006)
904 doi:10.1895/wormbook.1.105.1.

88. Savitzky, Abraham. & Golay, M. J. E. Smoothing and Differentiation of Data by Simplified Least Squares Procedures. *Anal. Chem.* **36**, 1627–1639 (1964).

89. Wagner, T. & Eglinger, J. thorstenwagner/ij-particlesizer: v1.0.9 Snapshot release. Zenodo https://doi.org/10.5281/ZENODO.820296 (2017).

90. Schindelin, J. *et al.* Fiji: an open-source platform for biological-image analysis. *Nat. Methods* **9**, 676–682 (2012).

91. Schnitzbauer, J., Strauss, M. T., Schlichthaerle, T., Schueder, F. & Jungmann, R. Super-resolution microscopy with DNA-PAINT. *Nat. Protoc.* **12**, 1198–1228 (2017).

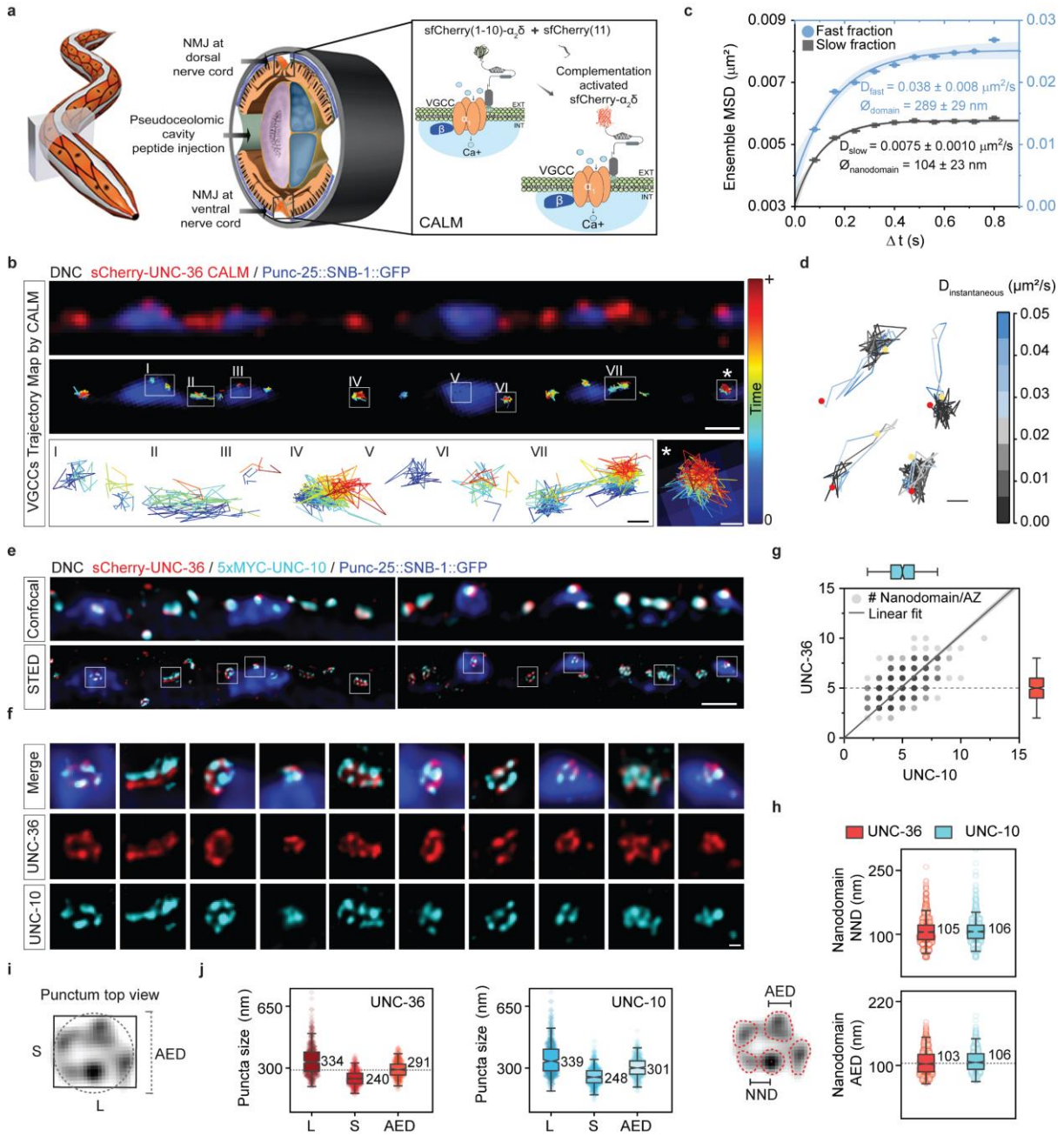

Figure 1. **N-type VGCCs exhibit two distinct diffusive behaviors within multiple nanodomains that correlate with UNC-10 at AZ.**

(a) Schematic of CALM by pseudocoelomic microinjection of synthetic sfcherry (11) peptides to activate extracellular split sfCherry (1-10) tagged to UNC-36 and detect surface-localized VGCC complexes at *C. elegans* NMJ. **(b)** Sum projection of a dual-color SM CALM movie by HILO light sheet imaging of sCherry-UNC-36 (red) along a dorsal nerve cord (DNC) marked with GABAergic Punc-25::SNB-1::GFP (blue, top). Corresponding VGCC trajectory maps color-coded by time (Tmin = blue; Tmax = red, middle) and zoom of selected insets (bottom). Scale bars, 1 µm (middle) and 100 nm (bottom). **(c)** Ensemble mean square displacement (MSD ± SEM) of slow (black squares) and fast (blue dots) fractions for VGCCs (n = 42,391; 58 animals). MSD curves

are fitted with a confined 2D diffusion model and the fit 95% confidence bands are shown together with the diffusion coefficient (D ± SEM) and the domain diameter (∅ ± localization precision) for each fraction. **(d)** Representative trajectories of heterogeneous VGCC diffusive behaviors color-coded by instantaneous diffusion coefficients ($D_{instantaneous}$). Trajectory start: yellow dot; trajectory stop: red dot; scale bar: 100 nm. **(e)** Confocal and dual-color STED images of immunostained surface sCherry-UNC-36 (red) and 5xMYC-UNC-10 (cyan) along dorsal nerve cords (DNC) marked by Punc-25::SNB-1::GFP (blue). Scale bars, 1 µm. **(f)** Zoomed insets of STED images in **(e)**. Scale bars, 100 nm. **(g)** Correlation between the number of UNC-36 (red) and UNC-10 (cyan) nanodomains per AZ (n = 516; 10 animals). Linear regression indicates proportional scaling (y=1.03x, R^2: 0.932). Notched boxes: median ± interquartile range (IQR); whiskers: 1.5xIQR. Dashed line marks the median number of UNC-36 nanodomains. **(h)** Nearest-neighbor distance (NND) and area-equivalent circular diameter (AED) of nanodomains for UNC-36 (red; n =1416 NND; 993 AED, 10 animals) and UNC-10 (cyan; n = 1454 NND; 786 AED; 10 animals). Notched boxes: median ± IQR; whiskers: 1.5xIQR. Dashed line marks the confinement size of the slow regime for VGCCs in (C). **(i, j)** Puncta sizes of UNC-36 (red) and UNC-10 (cyan) (n = 516; 10 animals). Notched boxes: median ± IQR; whiskers: 1.5xIQR. Dashed line marks the confinement size of the fast regime for VGCCs in (c).

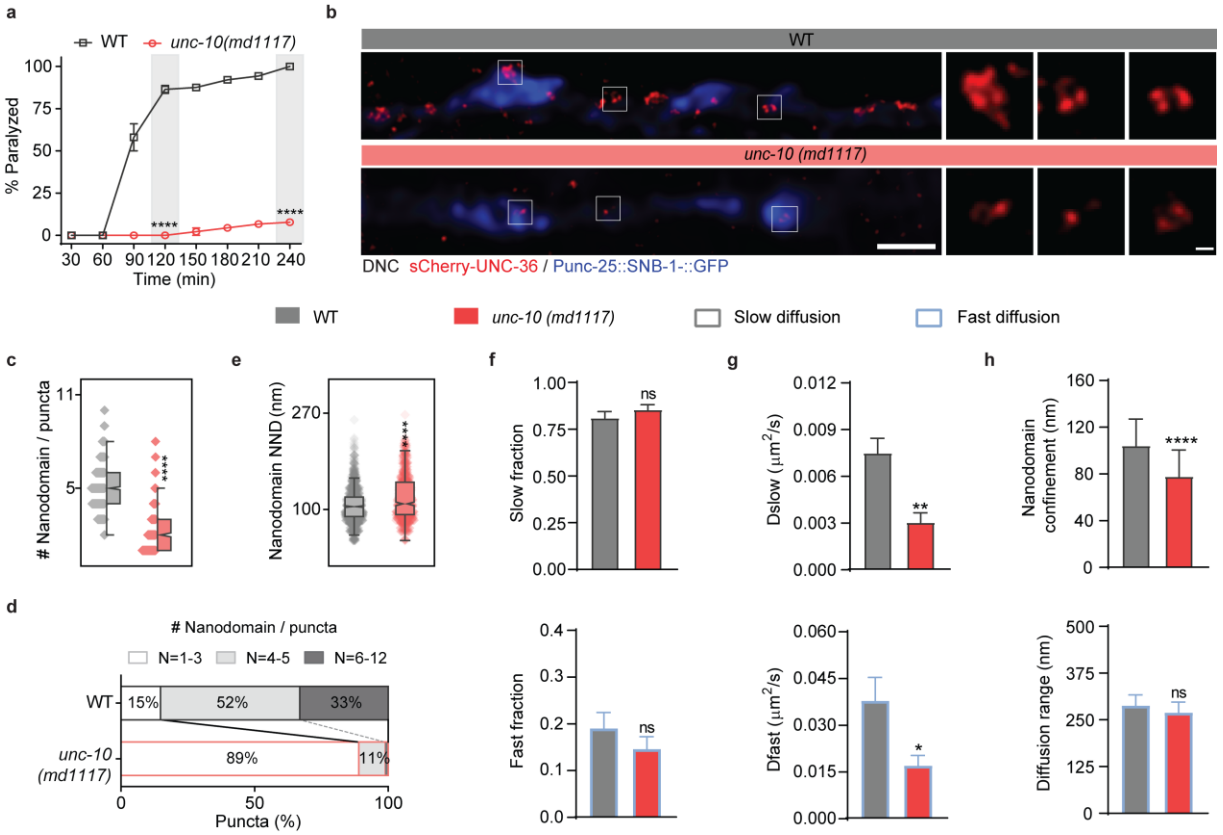

Figure 2. UNC-10 enhances VGCCs diffusion and promotes the multi-nanodomain organization of VGCC.

(a) Percentage of paralyzed animals over time (mean ± SEM) in aldicarb-sensitivity assays, comparing WT and *unc-10(md1117)* genotypes (n = 90). Two-way ANOVA and Tukey's tests, ****p<0.0001. **(b)** Representative STED images of immunostained surface sCherry-UNC-36 (red) overlayed with confocal images of Punc-25::SNB-1::GFP (blue) at the dorsal nerve cords of WT or *unc-10(md1117)* animals. Scale bars, 1 µm and 100 nm for insets. **(c-e)** Number (c), distribution (d) and nearest-neighbor distance NND (e) of UNC-36 nanodomains per diffraction-limited puncta in WT (gray; n = 1076 puncta; 1416 NND; 10 animals) and *unc-10 (md1117)* mutants (red; n = 634 puncta; 855 NND; 7 animals). Notched boxes: median ± interquartile range (IQR); whiskers: 1.5xIQR. Comparisons to WT by Kruskal-Wallis and Dunn's test, ****p < 0.0001. **(f-h)** Mobility of VGCCs in WT (gray; n= 42,391 trajectories; 58 animals) and *unc-10 (md1117)* mutant (red; n= 18,645 trajectories; 34 animals) with fractions (f, mean ± SEM), diffusion coefficients (g, mean ± SEM), and nanodomain confinement size or diffusion range (h, mean diameter ± localization precision) for the channels' slow (top row, black) and fast (bottom row, blue) diffusive behaviors. Comparisons to WT by two-tailed T-test. ****p < 0.0001; **p<0.01; *p<0.05; ns, not significant.

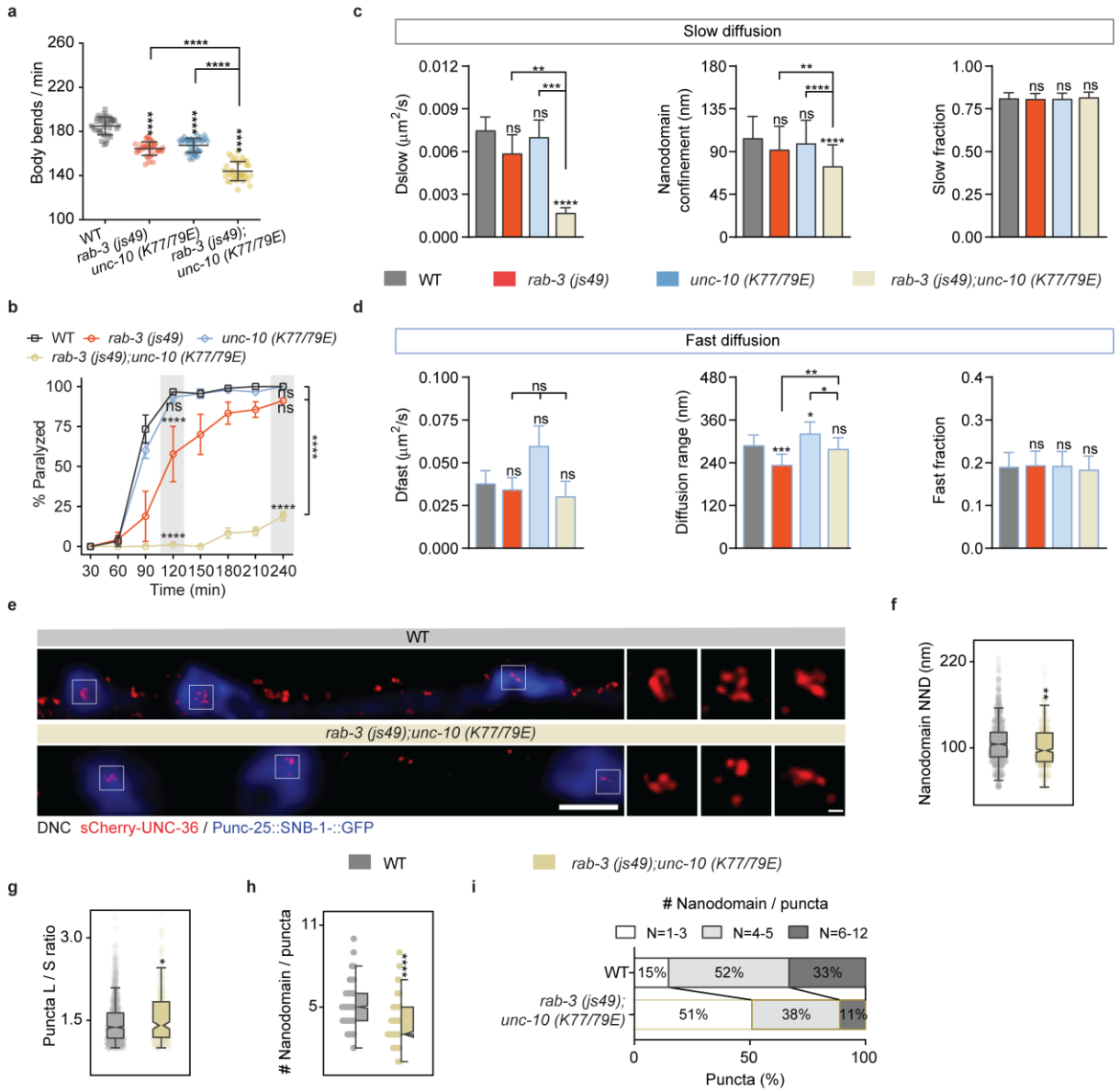

Figure 3. The mobility and spatial organization of nanodomain-associated VGCCs is regulated by UNC-10/RIM mediated SV coupling

(a) Numbers of body bending per min (mean ± SD) in trashing assays for animals (n = 36) of indicated genotypes. Comparisons by Kruskal-Wallis and Dunn's test, ****p < 0.0001. **(b)** Percentage of paralyzed animals over time (mean ± SEM) in aldicarb-sensitivity assays, for the indicated genotypes (n = 90). Comparisons to WT at time points by two-way ANOVA and Tukey's tests, ****p<0.0001; ns, not significant. **(c-d)** Mobility of VGCCs in WT (gray; n = 42,391 trajectories; 58 animals), *rab-3(js49)* (red; n = 33,175 trajectories; 107 animals), *unc-10 (K77/79E)* (blue; n = 29,278 trajectories; 26 animals) and *rab-3; unc-10(K77E/K79E)* mutants (brown; n = 24,455 trajectories; 19 animals), including diffusion coefficients (mean ± SEM), nanodomain confinement size or diffusion range (mean diameter ± localization precision) and fractions (mean ± SEM) for the channels' slow (c) and fast (d) diffusive behaviors. Comparisons by two-tailed T-test. ****p<0.0001; ***p<0.001; **p<0.01; *p<0.05; ns, not significant. **(e)** Representative STED

995 images of immunostained surface sCherry-UNC-36 (red) overlayed with confocal images of Punc-
996 25::SNB-1::GFP (blue) at the dorsal nerve cords of WT or *rab-3; unc-10(K77E/K79E)* animals.
997 Scale bars, 1 µm and 100 nm for insets. **(f-i)** Quantifications of UNC-36 nanodomain nearest-
998 neighbor distance NND (f), puncta long/short axe ratio (g), nanodomain numbers per puncta (h)
999 and their distribution (i) in STED images from WT (gray; n = 1416 NND; 1076 puncta; 10 animals)
1000 and *rab-3; unc-10(K77E/K79E)* mutants (brown; n = 509 NND; 244 puncta; 8 animals). Notched
1001 boxes: median ± interquartile range (IQR); whiskers: 1.5xIQR. Comparisons to WT by Kruskal-
1002 Wallis and Dunn's test, ****$p < 0.0001$; **$p<0.01$; *$p<0.05$.
1003

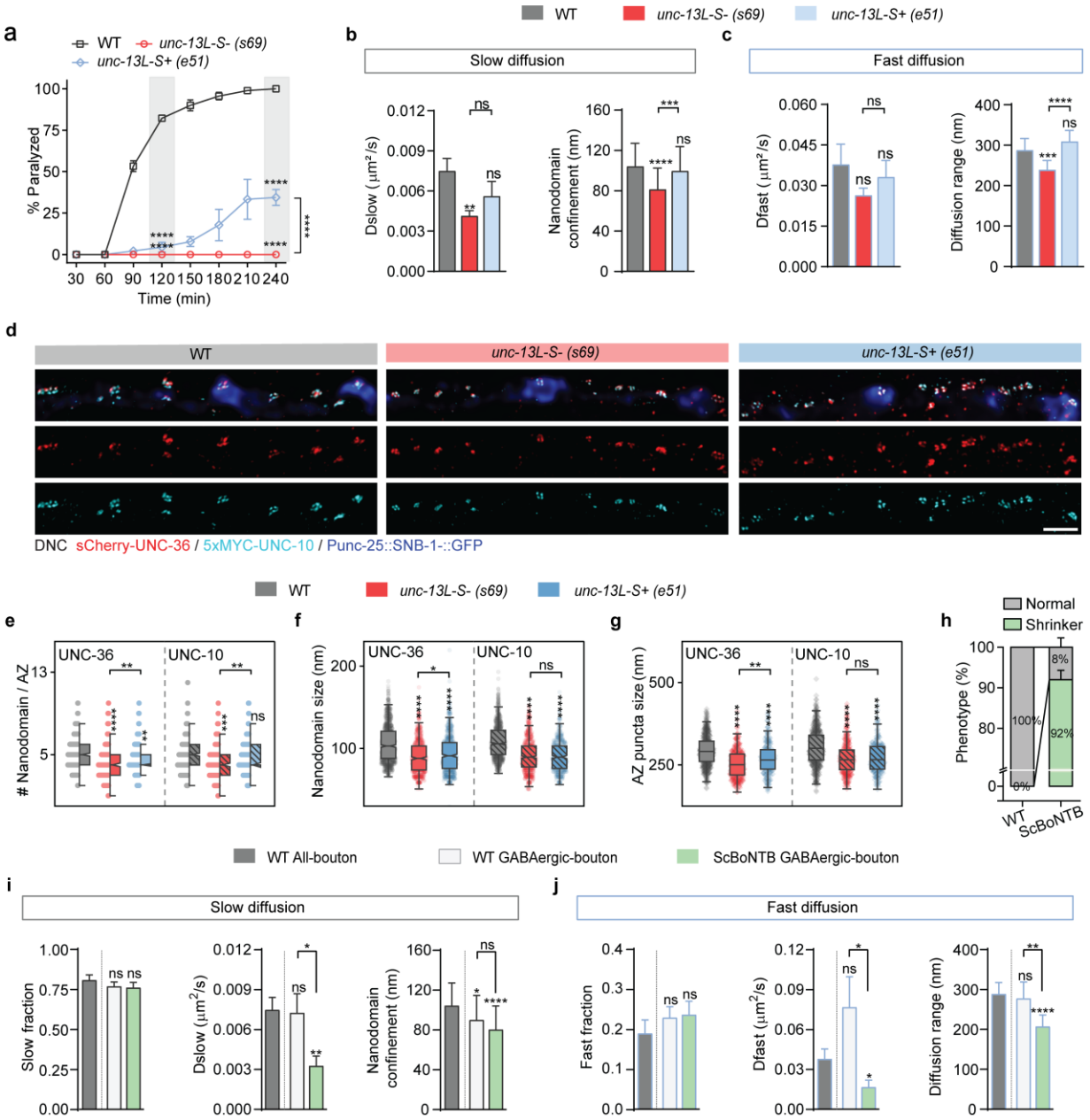

Figure 4. The mobility and AZ organization of VGCCs is governed by SV priming and SNARE complex assembly.

(a) Percentage of paralyzed animals over time (mean ± SEM) in aldicarb-sensitivity assays, for the indicated genotypes (n = 90). Comparisons to WT at time points or across genotypes at t = 240 min by two-way ANOVA and Tukey's tests, ****p<0.0001. **(b-c)** Mobility of VGCCs in WT (gray; n = 42,391 trajectories; 58 animals), *unc-13L-S- (s69)* (red; n = 31,355 trajectories; 35 animals) and *unc-13L-S+ (e51)* mutants (blue; n = 19,899 trajectories; 34 animals), including diffusion coefficients (mean ± SEM) and nanodomain confinement size or diffusion range (mean diameter ± localization precision) for the channels' slow (b) and fast (c) diffusive behaviors. Comparisons by two-tailed T-test. ****p<0.0001; ***p<0.001; **p<0.01; *p<0.05; ns, not significant. **(d)** Representative dual-color STED images of immunostained surface sCherry-UNC-36 (red) and

5xMYC-UNC-10 (cyan) overlayed with confocal images of Punc-25::SNB-1::GFP (blue) at the dorsal nerve cords of WT, *unc-13L-S- (s69)* and *unc-13L-S+ (e51)* animals. Scale bars, 1 µm. **(e-g)** Quantifications of UNC-36 and UNC-10 nanodomain numbers per AZ (e), nanodomain sizes (f), and puncta size at AZ (g) in WT (gray; n = 516 AZ puncta; 993 UNC-36 and 786 UNC-10 nanodomains; 10 animals), *unc-13L-S- (s69)* (red; n = 320 AZ puncta; 607 UNC-36 and 641 UNC-10 nanodomains; 6 animals) and *unc-13L-S+ (e51)* mutants (blue; n = 205 AZ puncta; 655 UNC-36 and 473 UNC-10 nanodomains; 4 animals). Notched boxes: median ± interquartile range (IQR); whiskers: 1.5xIQR. Comparisons by Kruskal-Wallis and Dunn's test, ****$p < 0.0001$; **$p<0.01$; *$p<0.05$; ns, not significant. **(h)** Percentage of animals displaying normal (grey) or "shrinker" (green) locomotory phenotypes (mean ± SEM) in WT and transgenic animals expressing ScBoNTB in GABAergic synapses (n = 50), over 3 independent batches of animals. **(i-j)** Mobility of VGCCs in WT animals at all boutons (dark gray; n = 42,391 trajectories; 58 animals), in WT animals at GABAergic boutons only (light gray; n = 19,034 trajectories; 42 animals) and in ScBoNTB-expressing animals at GABAergic boutons only (green; n = 11,549 trajectories; 36 animals), including fractions (mean ± SEM), diffusion coefficients (mean ± SEM), and nanodomain confinement size or diffusion range (mean diameter ± localization precision) for the channels' slow (i) and fast (j) diffusive behaviors. Comparisons by two-tailed T-test. ****$p<0.0001$; ***$p<0.001$; **$p<0.01$; *$p<0.05$; ns, not significant.

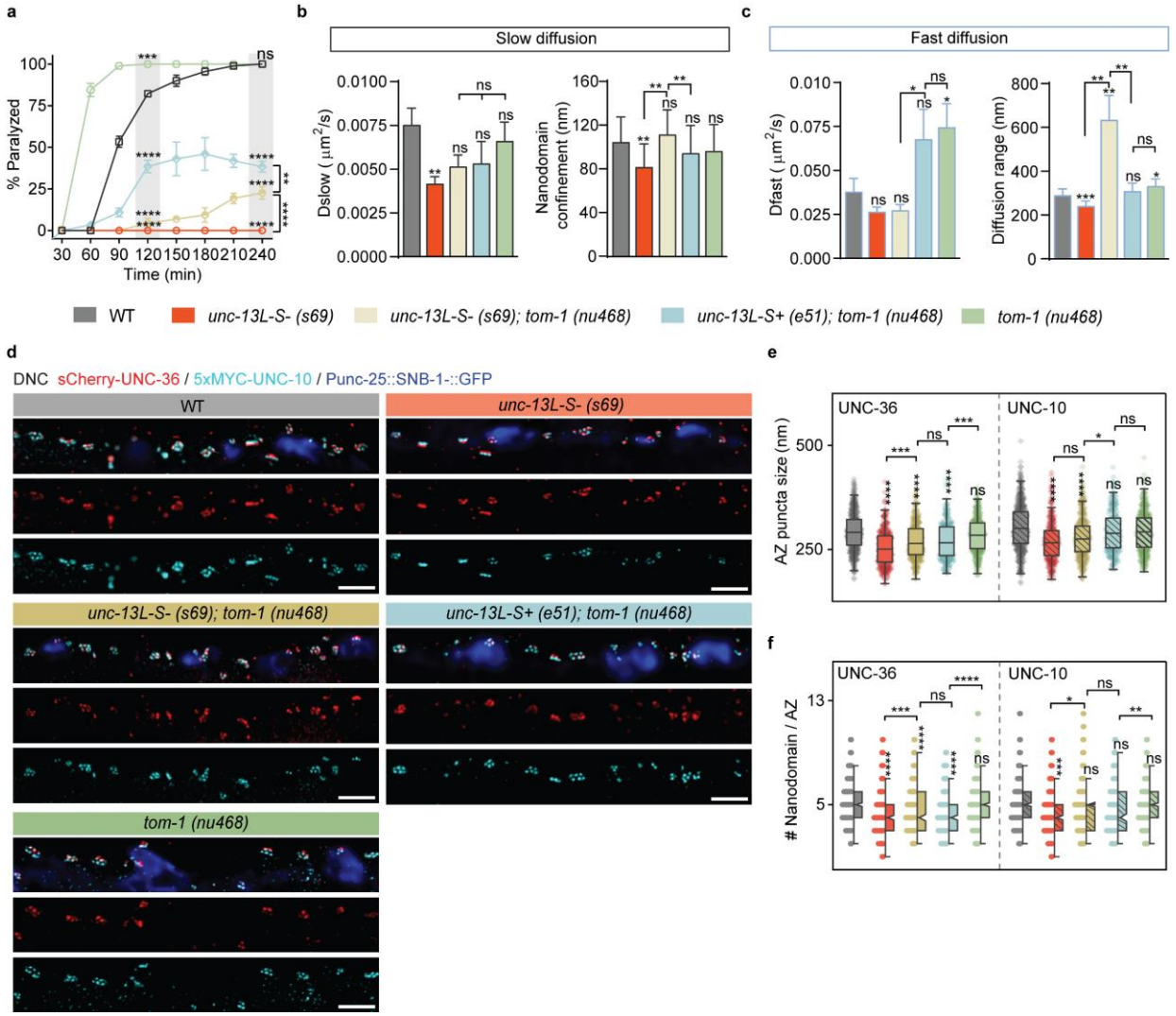

Figure 5. Distinct mobilities and nanodomain organization of VGCCs are differentially modulated by SV priming levels.

(a) Percentage of paralyzed animals over time (mean ± SEM) in aldicarb-sensitivity assays, for the indicated genotypes (n = 90). Comparisons to WT at time points t = 120min and across genotypes at t = 240 min by two-way ANOVA and Tukey's tests, ****p<0.0001; ***p<0.001; **p<0.01. **(b-c)** Mobility of VGCCs in WT (gray; n = 42,391 trajectories; 58 animals), *unc-13L-S- (s69)* (red; n = 31,355 trajectories; 35 animals), *unc-13L-S- (s69);tom-1(nu468)* (brown; n = 25,309 trajectories; 15 animals), *unc-13L-S+ (e51);tom-1(nu468)* mutants (cyan; n = 18,963 trajectories; 15 animals), and *tom-1(nu468)* mutants (green; n = 34,062 trajectories; 25 animals), including diffusion coefficients (mean ± SEM) and nanodomain confinement size or diffusion range (mean diameter ± localization precision) for the channels' slow (b) and fast (c) diffusive behaviors. Comparisons by two-tailed T-test. ***p<0.001; **p<0.01; *p<0.05; ns, not significant. **(d)** Representative dual-color STED images of immunostained surface sCherry-UNC-36 (red) and 5xMYC-UNC-10 (cyan) overlayed with confocal images of Punc-25::SNB-1::GFP (blue) at the dorsal nerve cords of WT, *unc-13L-S-(s69)*, *unc-13L-S-(s69);tom-1(nu468)*, *unc-13L-S+ (e51);tom-1(nu468)* and *tom-1(nu468)* animals. Scale bars, 1 µm. **(e-f)** Quantifications of UNC-36 and UNC-10 puncta size at

AZ (e) and nanodomain numbers per AZ (f) in WT (gray; n = 516 AZ puncta; 10 animals), *unc-13L-S-(s69)* (red; n = 320 AZ puncta; 6 animals), *unc-13L-S- (s69);tom-1(nu468)* (brown; n = 349 AZ puncta; 10 animals), *unc-13L-S+ (e51);tom-1(nu468)* mutants (cyan; n = 276 AZ puncta; 8 animals) and *tom-1(nu468)* mutants (green; n = 529 AZ puncta; 10 animals). Notched boxes: median ± interquartile range (IQR); whiskers: 1.5xIQR. Comparisons by Kruskal-Wallis and Dunn's test, ****$p < 0.0001$; *$p<0.05$; ns, not significant.

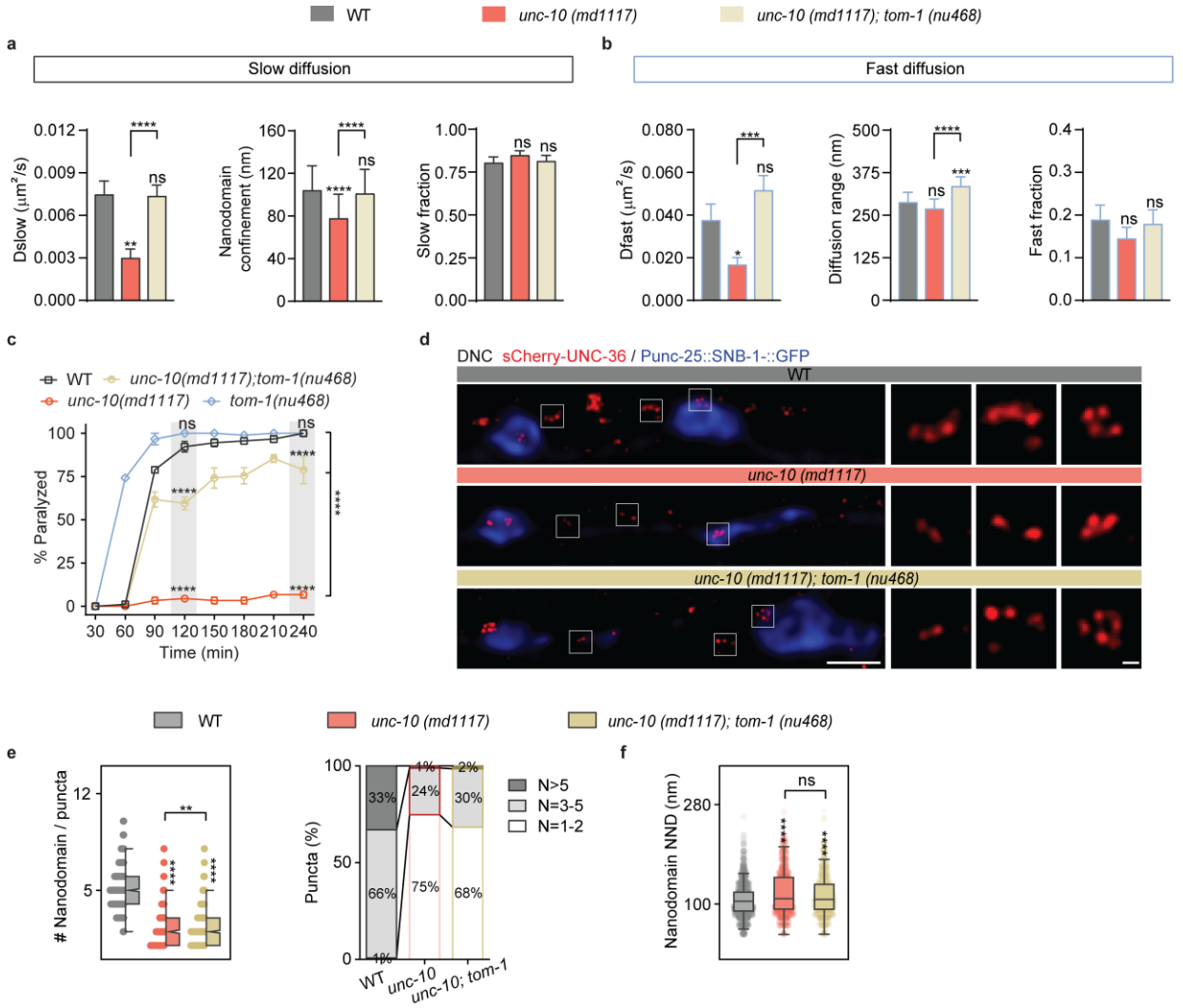

Figure 6. Primed SVs modulate the mobilities and multi-nanodomain organization of VGCCs downstream of UNC-10.

(a-b) Mobility of VGCCs in WT (gray; n= 42,391 trajectories; 58 animals); *unc-10 (md1117)* (red; n= 18,645 trajectories; 34 animals) and *unc-10(md1117);tom-1(nu468)* (brown; n = 20,882 trajectories; 26 animals) mutants, including diffusion coefficients (mean ± SEM), nanodomain confinement size or diffusion range (mean diameter ± localization precision) and fractions (mean ± SEM) for the channels' slow (a) and fast (b) diffusive behaviors. Comparisons by two-tailed T-test. ****p < 0.0001; ***p<0.001; **p<0.01; *p<0.05; ns, not significant. **(c)** Percentage of paralyzed animals over time (mean ± SEM) in aldicarb-sensitivity assays, for the indicated genotypes (n = 90). Comparisons to WT at time points or across genotypes at t = 240 min by two-way ANOVA and Tukey's tests, ****p<0.0001; ns, not significant. **(d)** Representative STED images of immunostained surface sCherry-UNC-36 (red) overlayed with confocal images of Punc-25::SNB-1::GFP (blue) at the dorsal nerve cords of WT, *unc-10 (md1117)* and *unc-10(md1117);tom-1(nu468)* animals. Scale bars, 1 μm and 100 nm for insets. **(e-f)** Quantifications of UNC-36 nanodomain numbers per puncta (e; left), distribution (e; right) and nearest-neighbor distance NND (f) in WT (gray; n = 1076 puncta; 1416 NND; 10 animals), *unc-10 (md1117)* (red; n = 634 puncta; 855 NND; 7 animals) and *unc-10(md1117);tom-1(nu468)* (brown; n = 1087 puncta; 748 NND; 8 animals) mutants. Notched boxes: median ± interquartile range (IQR); whiskers:

1.5xIQR. Comparisons by Kruskal-Wallis and Dunn's test, ****$p < 0.0001$; **$p<0.01$; ns, not significant.